Probing hot and dense nuclear matter with K^*, $\overline{K}^*$ vector mesons

Andrej Ilner,[1,2,*] Justin Blair,[3] Daniel Cabrera,[4] Christina Markert,[3] and Elena Bratkovskaya[5,1]

[1]*Institut für Theoretische Physik, Johann Wolfgang Goethe-Universität Frankfurt am Main, 60438 Frankfurt am Main, Germany*

[2]*Frankfurt Institute for Advanced Studies (FIAS), 60438 Frankfurt am Main, Germany*

[3]*The University of Texas at Austin, Physics Department, Austin, Texas C1600, USA*

[4]*Instituto de Física Corpuscular (IFIC), Centro Mixto Universidad de Valencia - CSIC, Institutos de Investigación de Paterna, Apartado de Correos 22085, E-46071 Valencia, Spain*

[5]*GSI Helmholtzzentrum für Schwerionenforschung GmbH Planckstrasse 1, 64291 Darmstadt, Germany*

(Received 30 June 2017; revised manuscript received 23 November 2018; published 28 February 2019)

We investigate the possibility of probing the hot and dense nuclear matter—created in relativistic heavy-ion collisions (HICs)—with strange vector mesons (K^*, $\overline{K}^*$). Our analysis is based on the nonequilibrium parton-hadron-string dynamics (PHSD) transport approach which incorporates partonic and hadronic degrees of freedom and describes the full dynamics of HIC on a microscopic level—starting from the primary nucleon-nucleon collisions to the formation of the strongly interacting quark gluon plasma (QGP), followed by dynamical hadronization of (anti)quarks as well as final hadronic elastic and inelastic interactions. This allows us to study the K^* and $\overline{K}^*$ meson formation from the QGP as well as the in-medium effects related to the modification of their spectral properties during the propagation through the dense and hot hadronic environment in the expansion phase. We employ relativistic Breit-Wigner spectral functions for the K^*, $\overline{K}^*$ mesons with self-energies obtained from a self-consistent coupled-channel G-matrix approach to study the role of in-medium effects on the K^* and $\overline{K}^*$ meson dynamics in heavy-ion collisions from FAIR/NICA to LHC energies. According to our analysis most of the final $K^*/\overline{K}^*$'s, that can be observed experimentally by reconstruction of the invariant mass of $\pi + K(\overline{K})$ pairs, are produced during the late hadronic phase and originate dominantly from the $K(\overline{K}) + \pi \rightarrow K^*(\overline{K}^*)$ formation channel. The amount of $K^*/\overline{K}^*$'s originating from the QGP channel is comparatively small even at LHC energies and those $K^*/\overline{K}^*$'s can hardly be reconstructed experimentally due to the rescattering of final pions and (anti)kaons. This mirrors the results from our previous study on the strange vector-meson production in heavy-ion collisions at RHIC energies. We demonstrate that $K^*/\overline{K}^*$ in-medium effects should be visible at FAIR/NICA and BES RHIC energies, where the production of $K^*/\overline{K}^*$'s occurs at larger net-baryon densities. Finally, we present the experimental procedures to extract the information on the resonance masses and widths by fitting the final mass spectra at LHC energies.

DOI: 10.1103/PhysRevC.99.024914

I. INTRODUCTION

The properties of hot and dense matter under extreme conditions, the origin of the phase transition from hadronic to partonic matter, and the formation of the quark-gluon plasma (QGP) are the subjects of extensive theoretical and experimental studies in the last decades. Such conditions—realized in nature during the "big bang" at the beginning of our universe—can be achieved nowadays in the laboratory in the collisions of heavy ions. There are presently several experimental facilities like the Schwerionensynchrotron (SIS) at the Gesellschaft für Schwerionenforschung (GSI), the Relativistic Heavy Ion Collider (RHIC) at the Brookhaven National Laboratory (BNL), and the Super-Proton Synchrotron (SPS) and the Large Hadron Collider (LHC) at the Conseil Européen pour la Recherche Nucléaire (CERN) which cover the range in invariant energy $\sqrt{s_{NN}}$ from a few GeV at SIS to ~5 TeV at LHC. Moreover, two further accelerators are under construction—the Facility for Antiproton and Ion Research (FAIR) as well as the Nuclotron-based Ion Collider fAcility (NICA)—which will become operational in the next years.

Due to confinement the QGP cannot be observed directly in experiments, which measure the final hadrons and leptons, and thus one needs reliable observables which carry information about the initial stages when the QGP has been created. Electromagnetic probes have the advantage that they practically do not suffer from final state interactions with the matter, however they are very rare and it is hard to detect them experimentally with high statistics. On the other hand hadrons are very abundant and rather easy to detect, however they participate in strong hadronic interactions after their creation which distort the information about their origin to some extent.

*ilner@fias.uni-frankfurt.de

In view of many hadronic probes the strange hadrons are of special interest since strangeness is not initially present in the colliding nuclei, but created during their collisions. Thus one hopes that it is easier to keep track of their production mechanism. In particular the strange vector-meson resonances K^* and $\overline{K}^*$ have been proposed as possibly sensitive probes [1,2]. The $K^*/\overline{K}^*$'s are expected to be produced at the partonic freeze-out [3] at relativistic energies and thus carry information about final QGP as well as the hadronic phase due to the final-state interactions.

Apart from detailed studies that have been performed by the STAR collaboration at RHIC [4–6], the $K^*/\overline{K}^*$ production has also been studied by the ALICE experiment at the LHC [7–25]. The measurement of the strange vector mesons $K^*/\overline{K}^*$ is quite challenging; the reconstruction goes via the decay channel $K^*(\overline{K}^*) \to \pi + K(\overline{K})$ by measuring the invariant mass of final pion and (anti)kaon pairs. However, $K^*/\overline{K}^*$'s are rather short-lived resonances and, even if they are produced at the hadronization of the QGP, they decay in the hadronic medium during the expansion of the system. The decay products—pions and (anti)kaons—suffer from hadronic final-state interactions—rescattering and absorption—which leads to a distortion of the $K^*/\overline{K}^*$'s spectra; furthermore, a sizable fraction of the decayed $K^*/\overline{K}^*$'s cannot be reconstructed at all. This is especially visible at LHC energies due to the large multiplicity of the final hadronic states. Additionally, due to the high meson density the $K^*/\overline{K}^*$'s can be often produced in the hadronic medium by formation of (anti)kaons and pions $\pi + K(\overline{K}) \to K^*(\overline{K}^*)$. Moreover, this mechanism turns out to be dominant as compared to the other production mechanisms of the $K^*/\overline{K}^*$ and the hadronization from the QGP in particular.

Thus, in order to understand $K^*/\overline{K}^*$ production and to provide a robust interpretation of the experimental results, one needs to address theoretical models. The most suitable models for that are transport approaches since only they can cover the whole complexity of the $K^*/\overline{K}^*$ dynamics from a microscopic point of view. We recall that such studies have been performed early with UrQMD [26,27] and EPOS3 [28] in Pb+Pb collisions at center-of-mass energies of $\sqrt{s_{NN}} =$ 17.3 GeV and $\sqrt{s_{NN}} = 2.76$ TeV, respectively.

Recently, we have studied the $K^*/\overline{K}^*$ production within the parton-hadron-string dynamics (PHSD) transport approach for relativistic energies of $\sqrt{s_{NN}} = 200$ GeV in Au+Au collisions at RHIC conditions [29]. There we have investigated the different mechanisms for the $K^*/\overline{K}^*$ production and have shown that most of the $K^*/\overline{K}^*$ measured experimentally at RHIC energies originate from $\pi + K(\overline{K})$ annihilation and overshine the direct production from the QGP which makes it quite difficult to use the $K^*/\overline{K}^*$ as a probe of the late partonic phase. Additionally, rescattering and absorption of final pions and (anti)kaons from $K^*/\overline{K}^*$ decay significantly and distort the final spectra. Moreover, in Ref. [29] we have studied for the first time the influence of in-medium effects on the $K^*/\overline{K}^*$ dynamics and final observables in the hadronic phase which are related to the modification of the $K^*/\overline{K}^*$ spectral properties during the propagation through the dense and hot hadronic medium. Such in-medium effects have been predicted by chiral models and G-matrix approaches and successfully been used for the description of the kaon K and antikaon $\overline{K}$ production [30–35]. In Ref. [29] we have implemented in the PHSD the in-medium effects of $K^*/\overline{K}^*$ resonances based on a G-matrix approach [36] as a function of the nuclear density [37]. We found that the influence of in-medium effects on the final $K^*/\overline{K}^*$ spectra is rather modest since most of $K^*/\overline{K}^*$'s are produced in the hadronic phase by $\pi + K(\overline{K})$ annihilation when the net-baryon density and the temperature have become low due to the rapid expansion of the system at $\sqrt{s_{NN}} = 200$ GeV.

The aim of this study is to investigate the dynamics of the $K^*/\overline{K}^*$ vector mesons in a wide energy range—from FAIR to LHC energies. We address the following questions in our study:

(i) Is the fraction of the $K^*/\overline{K}^*$'s produced from the QGP hadronization visible in the final observables? Indeed, due to the larger volume of the QGP at the LHC (compared to the RHIC energies), the total production of $K^*/\overline{K}^*$'s from the QGP is enhanced. However, the meson multiplicity at LHC is also much larger than at RHIC, thus the $\pi + K(\overline{K})$ annihilation mechanism would be also enhanced. Accordingly, the task is to give a quantitative answer to this issue.

(ii) What is the role of the final-state interaction on the $K^*/\overline{K}^*$ decay products, i.e., pions and (anti)kaons at the LHC?

(iii) What is the quantitative effect of in-medium modifications of the $K^*/\overline{K}^*$ properties on the final observables in HIC?

(iv) Which conditions, i.e., colliding energies, are best suited to study the $K^*/\overline{K}^*$ in-medium effects? In order to answer the last question we will go down in energy and study the $K^*/\overline{K}^*$ production also at the energies of the future FAIR/NICA and BES program at RHIC.

(v) How can one subtract the information on the medium effects from the observables using experimental methods? For that we will consider PHSD events in the same fashion as experimental data and apply the experimental extraction and fitting procedures.

Throughout this paper the following convention will be used: strange vector mesons consisting of an antistrange quark, i.e., $K^{*+} = (u\bar{s})$ and $K^{*0} = (d\bar{s})$, will be referred to as $K^* = (K^{*+}, K^{*0})$, while for mesons with a strange quark, i.e., $K^{*-} = (\bar{u}s)$ and $\overline{K}^{*0} = (\bar{d}s)$, the convention $\overline{K}^* = (K^{*-}, \overline{K}^{*0})$ will be used. Often we will use a notation $K^*/\overline{K}^*$ for K^* and $\overline{K}^*$. Also in the text we often express masses in the units of GeV or MeV assuming GeV/c^2 or MeV/c^2.

The structure of this study is as follows: In Sec. II we will give a short recall of the PHSD transport approach. In Sec. III the $K^*/\overline{K}^*$ vector-meson resonance in-medium properties will be shortly discussed, i.e., spectral functions calculated from a state-of-the-art G-matrix model as well as the implementation of these spectral functions into PHSD. In Sec, IV the properties and the dynamics of the $K^*/\overline{K}^*$ vector-meson resonance are investigated within PHSD for Pb+Pb collisions at LHC energies. Furthermore, the different production channels, the

actual baryon densities, and the in-medium effects of the $K^*/\overline{K}^*$ spectral functions are analyzed in detail. In Sec. V our results are presented and compared to the experimental data; in the first part we compare our results with data from $p+p$ collisions at LHC; the second part contains a detailed comparison of PHSD results with data from Pb+Pb collisions at LHC energies from the ALICE collaboration. In Sec. VI we use PHSD to obtain results for lower center-of-mass energies of $\sqrt{s_{NN}} = 10$ GeV to give predictions for the $K^*/\overline{K}^*$ in-medium dynamics at the future FAIR and NICA. In Sec. VII we discuss the experimental procedure to extract in-medium mass and width of a resonance. Finally, we summarize our findings in Sec. VIII.

II. PHSD TRANSPORT APPROACH

Our study is based on the Parton-Hadron-String Dynamics (PHSD) approach, which is a microscopic covariant dynamical approach for strongly interacting systems in and out of equilibrium [38,39]. The PHSD incorporates both partonic and hadronic degrees of freedom as well as the transition from the hadronic to the partonic phase, the QGP phase in terms of strongly interacting quasiparticles with further dynamical hadronization, and final hadronic interactions in the late stage; thus, PHSD covers the full time evolution of a relativistic heavy-ion collision on a microscopic level. The dynamical description of the strongly interacting system is realized by solving the generalized off-shell Cassing's transport equations which are obtained from the Kadanoff-Baym equations [40–42] in first-order gradient expansion and go beyond the mean-field and on-shell Boltzmann approximation for the collision terms.

The theoretical description of the partonic degrees of freedom (quarks and gluons) is realized in line with the dynamical-quasiparticle model (DQPM) [42,43] and describes the properties of QCD in terms of resummed single-particle Green's functions. The three parameters of the DQPM are fitted to reproduce lattice QCD (lQCD) results in thermodynamical equilibrium [44,45] such as energy density, pressure, and entropy density; the real and imaginary parts of the parton self-energies are used to define the widths and pole positions of the spectral functions of quarks and gluons taken in relativistic Breit-Wigner form. The DQPM provides the properties of the partons, i.e., masses and widths in their spectral functions as well as the mean fields for gluons/quarks and their effective two-body interactions that are implemented in the PHSD. For details about the DQPM model and the off-shell transport approach we refer the reader to the reviews in Refs. [36,46]. We mention that in equilibrium the PHSD reproduces the partonic transport coefficients such as shear and bulk viscosities or the electric conductivity from lattice QCD (lQCD) calculations as well [36,47].

The hadronic part is governed by the hadron-string-dynamics (HSD) part of the transport approach [48,49]; the hadronic degrees of freedom include the baryon octet and decouplet, the 0^- and 1^- meson nonets, as well as higher resonances. In the beginning of relativistic heavy-ion collisions color-neutral strings (described by the LUND model [50]) are produced in highly energetic scatterings of nucleons from the impinging nuclei, i.e., two strings can form through primary NN collisions. These strings are dissolved into "prehadrons," i.e., unformed hadrons with a formation time of $\tau_F \sim 0.8$ fm/c in the rest frame of the corresponding string, except for the "leading hadrons." Those are the fastest residues of the string ends, which can reinteract (practically instantly) with hadrons with a reduced cross section in line with quark counting rules. If the energy density is below the critical value for the phase transition, which is taken to be $\mathcal{E}_C = 0.5$ GeV/fm^{-3} (e.g., in $p+p$ reactions or in the hadronic corona), prehadrons become real hadrons after the formation time $t_F = \tau_F \gamma$ (γ is the gamma factor of the prehadron) in the calculational frame (center-of-mass system of $A+A$) and interact with hadronic cross sections. If the local energy density is larger than the critical value for the phase transition $\mathcal{E}_C$, the prehadrons melt into (colored) effective quarks and antiquarks in their self-generated repulsive mean field as defined by the DQPM [46]. In the DQPM the quarks, antiquarks, and gluons are dressed quasiparticles and have temperature-dependent effective masses and widths which have been fitted to lattice thermal quantities such as energy density, pressure, and entropy density.

For the time evolution of the QGP phase off-shell transport equations with self-energies and cross sections from the DQPM are used. With the expansion of the fireball the probability that the partons hadronize increases strongly close to the phase boundary. The hadronization is carried out on the basis of covariant transition rates. The resulting hadronic system is then governed by the off-shell HSD dynamics with optionally incorporated self-energies for the hadronic degrees of freedom [51].

To summarize, the full evolution of a relativistic heavy-ion collision, from the initial hard NN collisions out of equilibrium up to the hadronization and final interactions of the resulting hadronic particles, is fully realized in the PHSD approach. We recall that PHSD has been successfully employed for $p+p$, $p+A$, and $A+A$ reactions ranging from SIS to LHC energies (cf. Ref. [36] and references therein). Furthermore, in Ref. [29] we have extended the PHSD approach to the explicit $K^*/\overline{K}^*$ resonance dynamics by implementing the in-medium effects in terms of density and temperature dependent spectral functions at the hadronization, production, and propagation of K^*, $\overline{K}^*$'s.

III. REMINDER OF K^*, $\overline{K}^*$ IN-MEDIUM EFFECTS AND IMPLEMENTATION IN PHSD

In this section we briefly recall our approach used for the implementation of in-medium effects in the PHSD for the off-shell dynamics of the strange vector-meson resonances K^* and $\overline{K}^*$ [29,37].

The in-medium properties of strange mesons in dense and hot nuclear matter are determined by the meson self-energies calculated based on chirally motivated effective field models implemented using the G-matrix approach. The G-matrix approach is a unitary self-consistent coupled-channel approach which, in this case, involves also vector mesons [52–54] within the hidden local symmetry approach [55–58]. We use the G-matrix approach from Ref. [59] to calculate the self-energy of the $\overline{K}^*$. The in-medium spectral functions

for K^* and $\overline{K}^*$ then are approximated by relativistic Breit-Wigner spectral functions [37] with density or temperature dependent effective masses and widths related to the real and imaginary parts of the G-matrix self-energies. These Breit-Wigner spectral functions are used in the PHSD for the off-shell production and propagation of the strange vector-meson resonances K^* and $\overline{K}^*$ in heavy-ion collisions [29].

We remind here that in Ref. [37] the K^* meson self-energy at threshold energy has been obtained within an effective Lagrangian [53]. The collisional part of the self-energy of the K^* stems from summing the forward K^*N scattering amplitude over the allowed nucleon states in the medium, schematically $\Pi^{\rm coll}_{K^*} = \sum_{\vec{p}} n(\vec{p}) T_{K^*N}$. Due to the absence of resonant states nearby, a $t\rho$ approximation is well justified at energies sufficiently close to threshold,

$$\Pi^{\rm coll}_{K^*} \simeq \alpha \frac{M_K}{M_{K^*}} M^2_{K^*} \left(\frac{\rho}{\rho_0}\right), \tag{1}$$

with $\alpha \simeq 0.13$.

The $\overline{K}^*$ collisional self-energy part was implemented by using a parametrization of the $\overline{K}^*$ self-energy and spectral function from Ref. [59], where a detailed analysis of the medium corrections and self-consistent evaluation of the in-medium $\overline{K}^* N$ scattering has been carried out.

For a realistic description of the production rates the decay width of the K^* and $\overline{K}^*$ needs to be accounted for, including the in-medium modifications of the decay products, too. Such effects are readily incorporated for the $\overline{K}^*$ within the G-matrix approach which we parametrize from Ref. [59]. For the K^*, instead, we evaluate explicitly its medium-modified $K^* \to K\pi$ decay width as follows [37]:

$$\Gamma_{V,\,\rm dec}(M,\rho) = \Gamma^0_V \left(\frac{M_V}{M}\right)^2 \frac{\int_0^{M-m_\pi} q^3(M, M_j, M_\pi) A_j(M_j,\rho)\, dM_j}{\int_{M_{\rm min}}^{M_V - m_\pi} q^3(M_V, M_j, M_\pi) A_j(M_j, 0)\, dM_j}. \tag{2}$$

The indices are $j = K$ and $V = K^*$. Furthermore $q(M, M_j, M_\pi) = \sqrt{\lambda(M, M_j, M_\pi)}/2M$ with $\lambda(x,y,z) = [x^2 - (y+z)^2][x^2 - (y-z)^2]$. Γ^0_V is the partial vector meson decay width and M_V is the pole mass of the resonance in vacuum. We use $\Gamma^0_{K^*} = 42$ MeV and $M_V = 892$ MeV [60] (and the same for $\overline{K}^*$); M_π is the pion mass. Equation (2) accounts for the in-medium modification of the resonance decay width by its decay products. In particular, we consider the fact that kaons (and antikaons) may acquire a broad spectral function in the medium, $A_j(M,\rho)$. As discussed in Ref. [37], the kaon spectral function A_K in Eq. (2) is a delta function in vacuum since the kaon is stable in vacuum with respect to the strong interaction, and to a good approximation the same can be kept at finite nuclear density by using an effective kaon mass $M^{*2}_K(\rho) = M^2_K + \Pi_K(\rho)$ with $\Pi_K(\rho) \simeq 0.13 M^2_K(\rho/\rho_0)$ [35,61,62].

Pions are assumed to stay as narrow quasiparticles with vacuum properties in the evaluation of $\Gamma_{V,\rm dec}$ throughout this work. However, we mention that the in-medium modification of the pion spectral function in hot and dense hadronic matter is an unsettled question (cf. [63]): while from the experimental side there is no clear evidence for the pion broadening in heavy-ion collisions, there are many different models with quite contradictory results—such as in Ref. [64] a very large width of pions at zero momentum (up to 200 MeV at $T = 150$ MeV) was predicted due to their interaction in a hot meson gas while according to Refs. [65,66] the pions are expected to experience small changes up to temperatures $T \sim 100$ MeV in hot matter with low baryonic content, which supports our approximation of on-shell pions. This topic requires further theoretical (as well as experimental) investigation which is beyond the scope of our present study.

The spectral function is proportional to the imaginary part of the vector-meson in-medium propagator and has the following form:

$$S_V(\omega,\vec{q};\rho) = -\frac{1}{\pi}{\rm Im}D_V(\omega,\vec{q};\rho) = -\frac{1}{\pi}\frac{{\rm Im}\,\Pi_V(\omega,\vec{q};\rho)}{\left[\omega^2 - \vec{q}^{\,2} - M^2_V - {\rm Re}\,\Pi_V(\omega,\vec{q};\rho)\right]^2 + [{\rm Im}\,\Pi_V(\omega,\vec{q};\rho)]^2}, \tag{3}$$

where $V = K^*, \overline{K}^*$ and Π_V is the sum of the decay and collisional self-energy.

In spite of the G-matrix spectral function (3) containing the full information on the in-medium properties of strange vector mesons, for the practical purpose of implementation of in-medium effects in the microscopic transport approach PHSD (K^* and $\overline{K}^*$ production and off-shell propagation) we approximate the G-matrix spectral function (3) by the relativistic Breit-Wigner spectral function [$A_V(M,\rho)$, $V = K^*, \overline{K}^*$] within the assumption of small momentum $\vec{q} \to 0$—see [37,67]:

$$A_V(M,\rho) = C_1 \frac{2}{\pi} \frac{M^2 \Gamma^*_V(M,\rho)}{\left[M^2 - M^{*2}_V(\rho)\right]^2 + [M\Gamma^*_V(M,\rho)]^2}, \tag{4}$$

where M is the invariant mass and C_1 is a constant fixed by normalization:

$$\int_0^\infty A_V(M,\rho)\, dM = 1. \tag{5}$$

Note that the dimension of $A(M)$ is GeV^{-1} since M is included in (5).

As mentioned above, the Breit-Wigner spectral function (4) follows from the spectral function from the G-matrix approach (3) when setting the three-momentum of the vector meson to zero,

$$A_V(M,\rho) = 2C_1 M S_V(M,\vec{0},\rho), \tag{6}$$

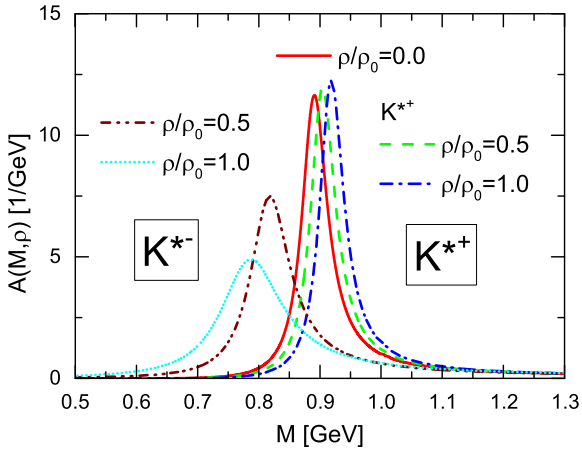

FIG. 1. The relativistic Breit-Wigner spectral functions $A(M, \rho)$ of the K^* and the $\overline{K}^*$ vs the invariant mass M for different nuclear baryon densities and in vacuum. The red solid line shows the vacuum $K^*/\overline{K}^*$ spectral functions, the green dashed line stands for the spectral function at baryon density of $\rho/\rho_0 = 0.5$, the blue dash-dotted line at $\rho/\rho_0 = 1.0$, the wine-colored dash-dot-dotted line at $\rho/\rho_0 = 0.5$, the light blue short-dotted line at $\rho/\rho_0 = 1.0$.

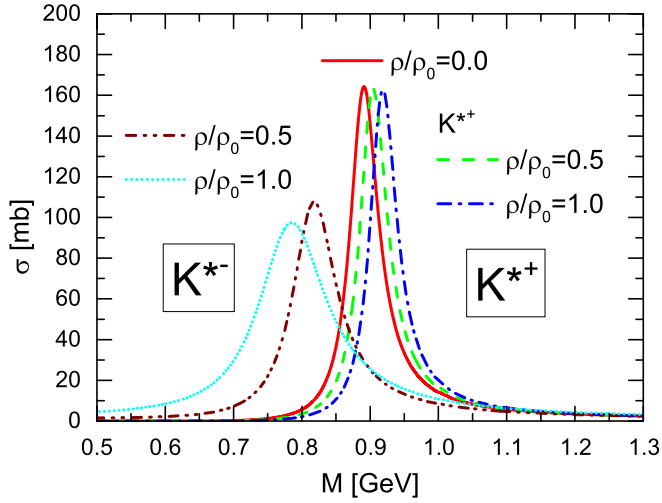

FIG. 2. The cross section σ for K^* production/annihilation is shown as a function of the invariant mass M for different baryon densities and in vacuum. The red solid line shows the vacuum $K^*/\overline{K}^*$ cross sections. The green dashed line shows the cross sections of $K^*/\overline{K}^*$ for a baryon density of $\rho/\rho_0 = 0.5$, the blue dash-dotted line at $\rho/\rho_0 = 1.0$, the wine-colored dash-dot-dotted line at $\rho/\rho_0 = 0.5$, the light blue short-dotted line at $\rho/\rho_0 = 1.0$.

i.e., neglecting the explicit momentum dependence. However, the self-energy is evaluated in such a way that it is at rest in the nuclear medium which is consistent with the aforementioned approximation. The in-medium mass M_V^* and the width Γ_V^* of the spectral function are related to the real and imaginary parts of the self-energy in the following way:

$$(M_V^*)^2 = M_V^2 + \mathrm{Re}\,\Pi_V(M_V^*, \rho),$$
$$\Gamma_V^*(M, \rho) = -\frac{1}{2M}\mathrm{Im}\,\Pi_V(M, \rho), \tag{7}$$

where M_V is the pole mass of the resonance in vacuum.

Figure 1 shows the spectral function for both the K^*s and $\overline{K}^*$s in vacuum and at finite nuclear density. While the vacuum spectral function has a width of 42 MeV and is centered around its respective pole mass of 892 MeV, a shift to higher and lower invariant masses can be seen for K^* and $\overline{K}^*$ at nonzero nuclear density. The K^* experiences a slight shift to higher invariant masses, the width is antiproportional to the nuclear density since the kaon also gets heavier. The threshold energy for K^* creation follows $M_{th} = M_K + M_\pi + \Delta M(\rho) \approx 0.633\ \mathrm{GeV} + \Delta M(\rho)$, with $\Delta M(\rho) \simeq \Pi_K(\rho)/2M_K$, which is approximately $0.06M_K$ at normal matter density.

The $\overline{K}^*$ on the other hand experiences a strong attraction and the spectral function is therefore shifted to lower invariant masses. The width gets considerably broader with increasing nuclear density. The threshold energy for the creation of a $\overline{K}^*$ decreases to $M_{th} \sim 2M_\pi$, i.e., an off-shell $\overline{K}^*$ can be created also at low invariant masses.

These in-medium effects have also an effect on the production rates of the K^* and the $\overline{K}^*$ in the hadronic phase of a heavy-ion collision. For the production cross section of K^* and $\overline{K}^*$ via $K + \pi$ or $\overline{K} + \pi$ annihilation we use the Breit-Wigner cross section [64,68–70] in relativistic form which can be written with the help of the in-medium spectral function (4) as

$$\sigma_{K^*(\overline{K}^*)}(M, \rho) = \frac{6\pi^2\, A_{K^*(\overline{K}^*)}(M, \rho)\, \Gamma^*_{K^*(\overline{K}^*)}(M, \rho)}{q(M, M_K, M_\pi)^2}. \tag{8}$$

Figure 2 shows the production cross section of $K^*/\overline{K}^*$ vector mesons at different baryon densities. The structure is similar to Fig. 1 depicting the spectral functions, i.e., the vacuum cross section is at the center, while the cross section shifted to higher invariant masses corresponds to the K^* and the cross section shifted to lower invariant masses corresponds to the $\overline{K}^*$. The $\overline{K}^*$ cross section follows the same trend as the spectral function, i.e., the cross section becomes smaller with increasing nuclear baryon density. However, for the K^* a reversed effect emerges as compared to the spectral function, i.e., the cross section of the K^* slightly decreases with increasing nuclear density due to a reduction of the phase space when the mass increases.

We note that in the present study we have omitted "thermal" in-medium effects related to a coupling to the hot mesonic medium since according to our previous study [37] such effects are small. This topic requires further detailed investigation since the meson density at the LHC energies is very high.

IV. $K^*/\overline{K}^*$ DYNAMICS IN PHSD

In this section we present our results on the on- and off-shell dynamics of the $K^*/\overline{K}^*$ within the PHSD transport approach at center-of-mass energies of $\sqrt{s_{NN}} = 2.76$ TeV in central Pb+Pb collisions. We investigate the evolution of the $K^*/\overline{K}^*$ abundance in time as well as the main contributing production channels. Furthermore, we compare the baryon density during the creation of the $K^*/\overline{K}^*$'s at

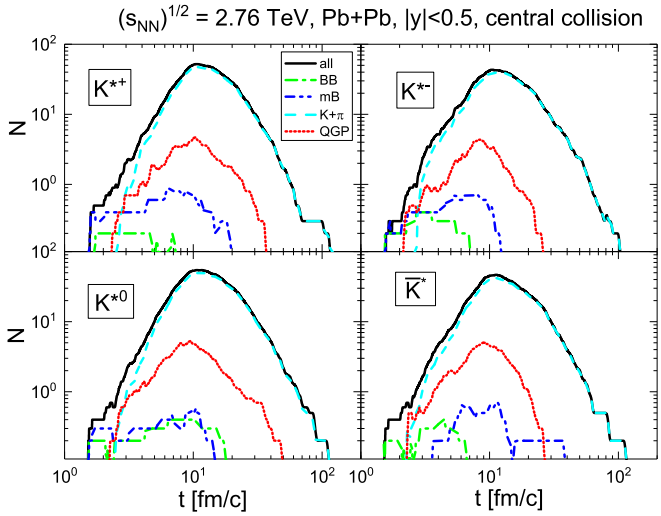

FIG. 3. The number $N(t)$ of formed strange vector mesons vs the time t for different production channels at midrapidity y in a central Pb+Pb collision at a center-of-mass energy of $\sqrt{s_{NN}} = 2.76$ TeV from PHSD calculations. The upper left panel (a) shows the channel decomposition for the K^{*+}, the upper right panel (b) for the K^{*-}, the lower left panel (c) for the K^{*0}, and the lower right panel (d) for the $\overline{K}^{*0}$. The color coding is the same for all of the four panels: the sum over all the production channels at given time t is shown as a black solid line. The dash-dotted green line shows the $K^*/\overline{K}^*$'s produced from baryon-baryon strings, the dash-dot-dotted blue line from meson-baryon strings, the dashed line from $K(\overline{K}) + \pi$ annihilations, and the short-dotted red line from the hadronization of the QGP.

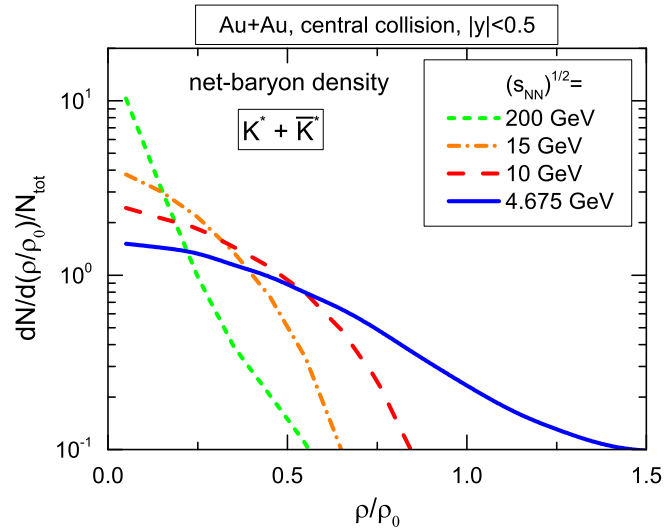

FIG. 4. The normalized net-baryon density distribution $dN/d(\rho/\rho_0)/N_{\rm tot}$ at the production point of $K^* + \overline{K}^*$'s for different collision energies at midrapidity ($|y| < 0.5$) as obtained from the PHSD calculations. The short-dashed green line shows the result for Au+Au at 200 GeV, short-dot-dashed orange line at 15 GeV, dashed red lineat 10 GeV, solid blue line at 4.675 GeV.

different energies. For a better understanding of the effects of experimental cuts we refer to our last study in Ref. [29].

We start with the time evolution of the $K^*/\overline{K}^*$ abundances. As seen from Fig. 3 the total number of formed $K^*/\overline{K}^*$'s from the all isospin channel is roughly the same, i.e., there is an approximately equal number of K^*'s and $\overline{K}^*$'s present at every time during the collision and expansion. The production by strings dominates at the very early stages of the collisions and very slowly decreases, although its relative contribution to the total number of K^*'s becomes negligibly small after about 10 fm/c. We note that the mesons coming from string decay are mainly dissolved to the QGP partons; they also can be "leading" mesons if they come from the ends of breaking string or stay as under the formation time in the corona of the collisions where the energy density is not high enough to form the QGP. Since in Fig. 3 only the formed mesons are shown, prehadrons and headings are not accounted for here. The contribution of the QGP is not very large either, especially when compared to the main production channel, i.e., the $K(\overline{K}) + \pi$ annihilation. The contribution of the QGP starts a few fm/c later in the collision, however, its overall effect does not exceed the contribution from strings. Almost at the same time, when the QGP starts to contribute to the total number of particles, $K^*/\overline{K}^*$'s also start to emerge from $K(\overline{K}) + \pi$ annihilations. However, this channel rises quickly and stays the dominant channel throughout the collision. Thus, we found that even at the LHC energy, in spite of the large volume of the created QGP, most of the K^*'s are produced by the resonant final-state interactions of $\pi + K(\overline{K})$, similar to the RHIC energies [29].

In view of the fact that K^*'s are produced dominantly in the final hadronic phase, the following questions arise: (i) Which baryon density is probed with K^*'s? (ii) Can one observe an in-medium modification of the K^* properties in the hadronic environment? (iii) Which energies are more suited for a robust observation? In order to answer these questions we show in Fig. 4 the normalized net-baryon density distribution $dN/d(\rho/\rho_0)/N_{\rm tot}$ at the $K^* + \overline{K}^*$'s production point for central Au+Au collisions at midrapidity ($|y| < 0.5$) for different collision energies of $\sqrt{s_{NN}} = 4.675$, 10, 15, and 200 GeV. As follows from Fig. 4, at high collision energies the $K^*/\overline{K}^*$'s are produced at rather low net-baryon density since the dominant production proceeds via $\pi + K$ annihilation (cf. Fig. 3) when the system is dominated by mesons with only a low amount of baryons and antibaryons. However, when decreasing the energy the fraction of $K^*/\overline{K}^*$'s created at larger density increases, such that for $\sqrt{s_{NN}} = 4.675$ GeV one can probe baryon densities even above normal nuclear matter density. Correspondingly, the in-medium effects are expected to be more pronounced at low energies (e.g., at FAIR and NICA or low BES RHIC).

V. RESULTS FROM PHSD AT LHC ENERGIES

In this section we will present the results for $K^*/\overline{K}^*$ production in heavy-ion collisions and pp reactions from the PHSD transport approach. We compare these results to experimental data measured by the ALICE collaboration at the LHC [7–25]. Since the net-baryon density at midrapidity is very small at the LHC energies, we discard here a consideration

of the in-medium effects and present the results for the "free" case here. We recall that in our in-medium scenario the modification of the $K^*/\overline{K}^*$ properties occurs due to the coupling to the baryonic medium while the coupling to antibaryons is discarded. However, at the LHC energies the antibaryon density at midrapidity is close to the baryon density, thus the expected in-medium modification of K^* and $\overline{K}^*$ properties would be small since the coupling to the antibaryons leads to the opposite effect compared to the coupling to the baryons for the vector interaction. A consistent consideration of the coupling to antibaryons requires a further extension of the in-medium model which is a subject of future studies.

A. "Decay" spectra versus "reconstructed" spectra

Some remarks on the $K^*/\overline{K}^*$ reconstruction procedure—experimental as well as theoretical—have to be made first:

(i) The ALICE collaboration measures the $K^{*0}/\overline{K}^*$ vector mesons through the hadronic decay channel: $K^{*0} \to \pi^{\pm} + K^{\mp}$. The daughter particles of the K^* can be tracked in the time projection chamber (TPC) which has a finite acceptance, i.e., the resolution and accuracy of the detector also needs to be taken into account. The main problem here is related to the fact that the decay products—pions and kaons—suffer from final-state interactions (FSIs) during the expansion phase: they can rescatter or may be absorbed. This leads to a substantial distortion of the reconstructed spectra which makes the physical interpretation of experimental results rather difficult. In our previous study [29] we have analyzed the influence of the FSI effects at RHIC energies, which were found to be significant. It is expected also to play an important role at the LHC energy.

(ii) The other problem with the experimental reconstruction of $K^*/\overline{K}^*$'s is related to the background subtraction. The $K^*/\overline{K}^*$ signal is obtained by taking all the viable decay channels into account and combining all pions and (anti)kaons from a single event. This will lead to the "real" $K^*/\overline{K}^*$ signal on a top of a very large background (uncorrelated spectrum) which is subtracted by a combinatorical method. The signal and the shape of the final $K^*/\overline{K}^*$ distribution is sensitive to the selected region around the $K^*/\overline{K}^*$ peak position in the mass distribution. However, as discussed above, due to the FSI the signal is distorted, thus a large fraction of $K^*/\overline{K}^*$'s cannot be reconstructed. Also experimental procedure to fit the signal and extract the information on K^*'s is model dependent as will be discussed in Sec. VII.

Contrary to experiment, in theoretical calculations we can follow (within the microscopic transport models) all $K^*/\overline{K}^*$'s in their history of production and decay. In Ref. [29] we have compared the PHSD spectra of $K^*/\overline{K}^*$'s at the decay point, i.e., "true" $K^*/\overline{K}^*$'s, with the reconstructed $K^*/\overline{K}^*$'s from the $\pi + K(\overline{K})$ decay channel as in experiment. Following the same strategy, in our present theoretical study we will call the $K^*/\overline{K}^*$'s spectra obtained directly at the decay point decayed spectra. When $K^*/\overline{K}^*$ decay to pions and (anti)kaons, we trace the collision history of the decay products: if pions and/or (anti)kaons scatter elastically, and finally both escape the fireball, we account for them in the reconstructed $K^*/\overline{K}^*$ spectra by summing their four-momenta. On the contrary, the pions and/or (anti)kaons which approach inelastic (or quasielastic charge exchange) reactions are lost for the reconstruction—for our theoretical model and for the real experimental reconstruction—since they did not escape the fireball and thus, did not reach the detector. We note, however, that in our reconstructed case—contrary to experiment—we do not have a "loss" of the signal due to misidentification, background subtraction, or experimental acceptances. Thus, we use here our analysis to illustrate the distortion of the spectra due to the final state interaction in the hadronic phase.

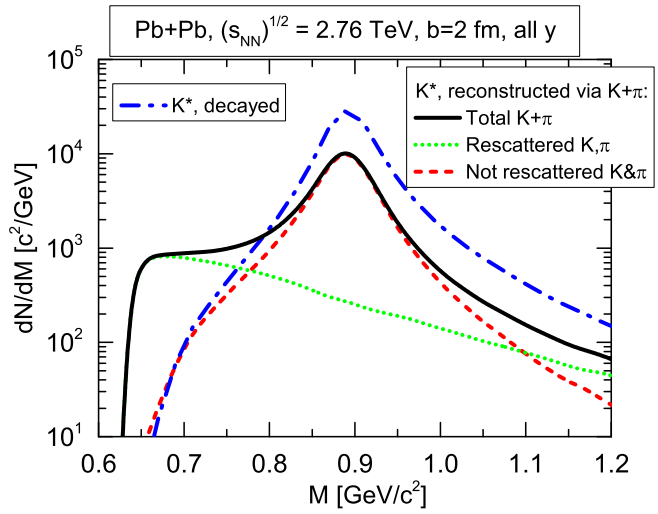

FIG. 5. The reconstructed $K^* = K^{*+} + K^{*0}$ mass distribution dN/dM via $K + \pi$ for Pb+Pb collision at impact parameter $b =$ 2 fm without cut in rapidity y at a center-of-mass energy $\sqrt{s_{NN}} =$ 2.76 TeV from the PHSD calculation: the green dotted line shows the reconstructed $K + \pi$ mass distribution for the case without rescattering of pions and kaons while the red dashed line stands for the case when pions and/or kaons rescatter elastically in the medium; the black solid line shows the sum of both contributions. The blue dot-dashed line stands for the decayed K^* spectra.

In Fig. 5 we show the reconstruction procedure for the K^* mass distribution dN/dM for Pb+Pb collision at impact parameter $b = 2fm$ at a center-of-mass energy $\sqrt{s_{NN}} =$ 2.76 TeV. For this illustrative plot we show the spectra without cut in rapidity (all y) in order to accommodate better statistics, however, we note that the cut in rapidity reduces the spectra by about a factor of 9. The green dotted line in Fig. 5 shows the reconstructed $K + \pi$ mass distribution for the case without rescattering of pions and kaons while the red dashed line stands for the case when pions and/or kaons rescatter elastically in the medium. One can see that the shape of the "not rescattered" $K + \pi$ mass spectrum are close to the shape of true, i.e., decayed K^* spectra (blue dot-dashed line). On the other hand the shape of the decayed K^* spectra follows the shape of the K^* spectral function weighted with

the occupation probability (a Boltzmann factor), which tilts the spectra a bit to lower masses and suppresses the high tail of the spectral function.

The rescattered $K+\pi$ contribution is rather flat and shifted to the lower mass region. This part of the spectrum cannot be identified experimentally in the $\overline{K}^*$ observables since it contributes to the subtracted combinatorial background which is fitted to the low and high mass region of the measured $\overline{K}+\pi$ mass distribution. Thus, experimentally the "signal" is selected under the peak of the $K+\pi$ mass distribution while the rest is not included in measured observables. In order to be close to the experimental situation we selected the mass region $M=[0.8, 1.0]$ GeV when comparing to the experimental data. In this mass range the contribution of the rescattered $K+\pi$ is less than 7% to the total reconstructed spectra. On the other hand only about 40% of the decayed K^*'s with the masses 0.8–1.0 GeV end up in the reconstructed spectra at the same mass region. Later we will show examples of reconstructed mass distributions keeping all true $K+\pi$ pairs from the decay of $K^*/\overline{K}^*$ resonances.

In Fig. 6 we present the differential mass distribution dN/dM for the vector kaons $K^{*+}+K^{*0}$ (a) and for vector antikaons $\overline{K}^{*-}+\overline{K}^{*0}$ (b) for central Pb+Pb collisions at $\sqrt{s_{NN}}=2.76$ TeV at midrapidity ($|y|<0.5$) from the PHSD calculations. Here we show the true $K^*/\overline{K}^*$ spectra, i.e., obtained directly at their decay point (solid black lines) and the reconstructed spectra from the final pions and kaons (solid orange lines with circles). Similar to Fig. 5 one can see a strong modification of the mass spectra: a shift to lower invariant masses and a reduction of the yield at the vacuum peak position. As said above, this modification arises from the rescattering and absorption of the final pions and kaons. Moreover, in Fig. 6 we show that at the LHC energy the main source of $K^*/\overline{K}^*$ mesons is the $\pi+K$ annihilation which is substantially larger than the fraction of $K^*/\overline{K}^*$ produced in the hadronization of the QGP. We note that the relative fraction of the $K^*/\overline{K}^*$ from the annihilation at LHC is even larger than at RHIC since the total abundance of mesons is much larger at the LHC energy.

Furthermore, in Fig. 7 we show the differential $K^*/\overline{K}^*$ mass spectrum dN/dM for central Pb+Pb collisions at midrapidity ($|y|<0.5$) and $\sqrt{s_{NN}}=2.76$ TeV from the PHSD calculation for different p_T bins. Panels (a) and (b) show the spectrum for the reconstructed $K^*/\overline{K}^*$s while panels (c) and (d) show the spectrum for the decayed $K^*/\overline{K}^*$s. One can see that the shape of the "decayed" $K^*/\overline{K}^*$'s mass spectra is rather similar for the different p_T bins while the reconstructed spectra changes differently in different p_T bins: the distortion of the spectra is strongest for low p_T. That is due to the fact that the low p_T pions and kaons suffer from stronger and more frequent rescattering and absorption.

The influence of the experimental reconstruction procedure and experimental cuts—due to the detector acceptance—on the p_T spectra is shown in Fig. 8. Here the PHSD results for the transverse momentum spectrum $d^2N/(dydp_T)$ of $(K^{*0}+\overline{K}^{*0})/2$ for a central Pb+Pb collision at midrapidity $|y|<0.5$ at $\sqrt{s_{NN}}=2.76$ GeV are shown in comparison to

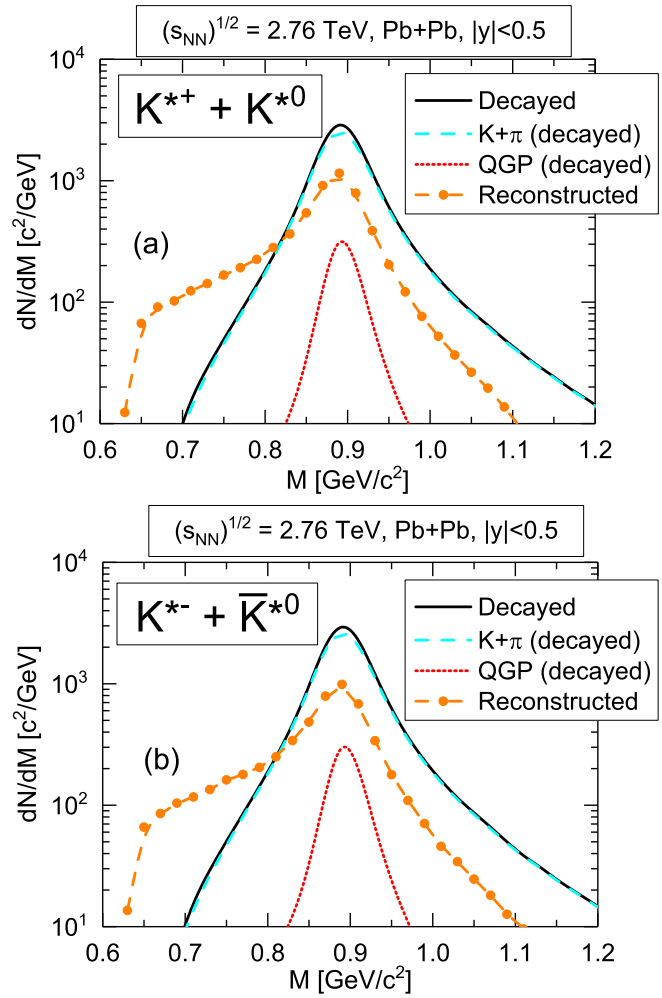

FIG. 6. The differential mass distribution $\frac{dN}{dM}$ for the vector kaons $K^{*+}+K^{*0}$ (a) and for vector antikaons $\overline{K}^{*-}+\overline{K}^{*0}$ (b) for central Pb+Pb collisions at a center-of-mass energy of $\sqrt{s_{NN}}=2.76$ TeV at midrapidity ($|y|<0.5$) from the PHSD calculations. The solid orange lines with circles show K^*'s and $\overline{K}^*$'s reconstructed from final kaon and pion pairs while all of the other lines represent the different production channels at the decay point of the K^* and $\overline{K}^*$, i.e., the black lines show the total number of the K^*'s and $\overline{K}^*$'s at their decay points, while the light blue dashed lines show the decayed K^*'s and $\overline{K}^*$'s that stem from the $\pi+K$ annihilation and the short-dotted red lines indicate the decayed K^*'s and $\overline{K}^*$'s which have been produced during the hadronization of the QGP.

the experimental data from the ALICE collaboration [16]: the solid green line with squares shows the spectrum calculated from $K^*/\overline{K}^*$'s at the decay point while the dashed red line with stars shows the reconstructed spectrum from final (matching) kaons and pions. Similar to our finding (at RHIC energies) in Ref. [29] we see a strong reduction of the low p_T spectra which is due to the "loss" of signal stemming from the rescattering/absorbtion mechanisms and the experimental cuts applied; in particular the restriction on the invariant mass range for the $K^*/\overline{K}^*$ reconstruction contributes to this distortion. Finally the reconstructed spectrum is much harder

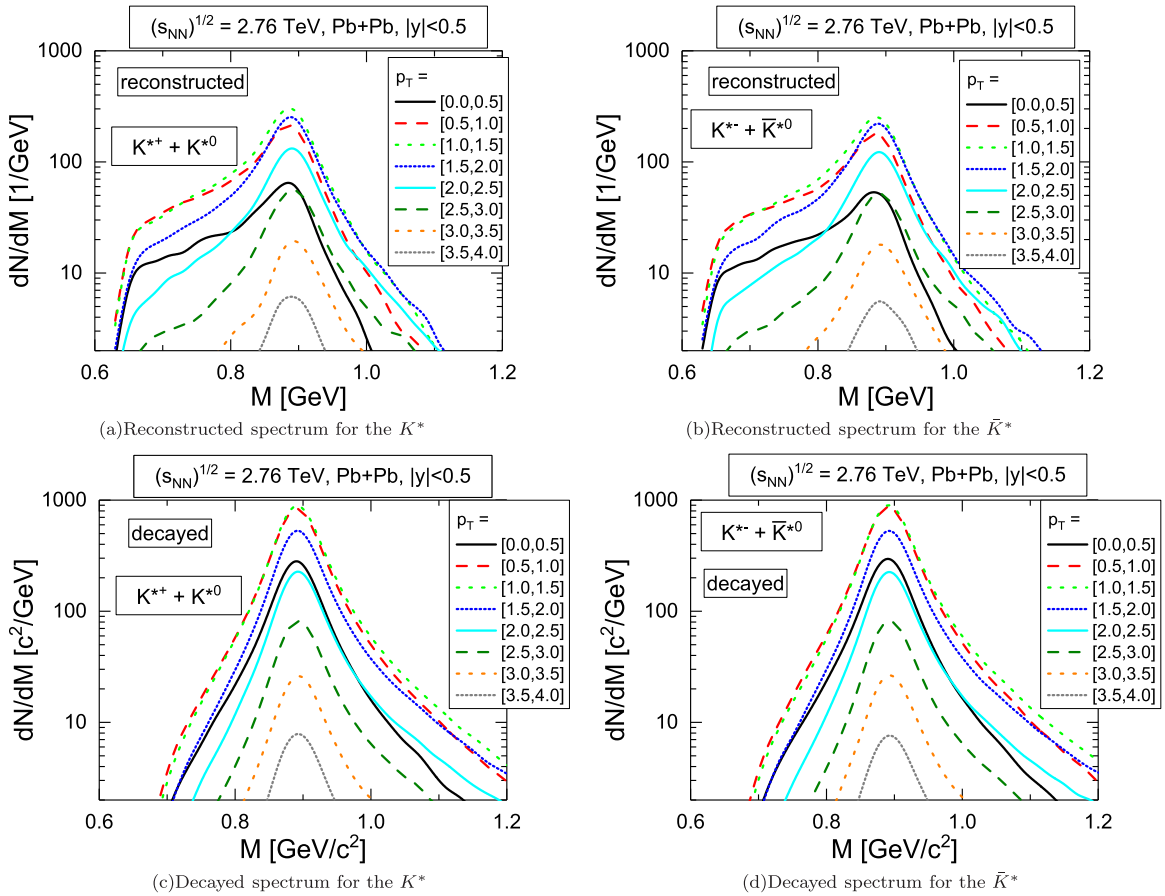

(a)Reconstructed spectrum for the K^*

(b)Reconstructed spectrum for the $\bar{K}^*$

(c)Decayed spectrum for the K^*

(d)Decayed spectrum for the $\bar{K}^*$

FIG. 7. The differential $K^*/\overline{K}^*$ mass spectrum dN/dM for central Pb+Pb collision at midrapidity ($|y| < 0.5$) at a center-of-mass energy $\sqrt{s_{NN}} = 2.76$ TeV from the PHSD calculation for different p_T bins. Panels (a) and (b) show the spectrum for the reconstructed $K^*/\overline{K}^*$s while panels (c) and (d) show the spectrum for the decayed $K^*/\overline{K}^*$s. Panels (a) and (c) show results for the K^* mesons while panels (b) and (d) show results for the $\overline{K}^*$ mesons. All panels show the differential mass spectrum taken from the K^*'s and $\overline{K}^*$'s in specific transverse momentum ranges of $p_T = [0.0, 0.5]$ GeV (solid black line), $p_T = [0.5, 1.0]$ GeV (dashed red line), $p_T = [1.0, 1.5]$ GeV (short-dashed green line), $p_T = [1.5, 2.0]$ GeV (short-dotted blue line), $p_T = [2.0, 2.5]$ GeV (solid light blue line), $p_T = [2.5, 3.0]$ GeV (dashed olive line), $p_T = [3.0, 3.5]$ GeV (short-dashed orange line), $p_T = [3.5, 4.0]$ GeV (short-dotted grey line).

than the true (decayed) one. Furthermore, we find that at the LHC energy—similar to the RHIC energies—the influence of the FSI on the final $K^*/\overline{K}^*$ spectra is getting smaller with decreasing system size and becomes negligible for $p + p$ collisions where the reconstructed and decayed spectra are almost identical.

In Fig. 9 we show the comparison of the PHSD results (red solid line with stars) for the transverse momentum spectrum $\frac{1}{N_{\rm inel}} \frac{d^2N}{dy dp_T}$ of the neutral $(K^{*0} + \overline{K}^{*0})/2$ mesons for $p + p$ collisions at midrapidity $|y| < 0.5$ at LHC energies of $\sqrt{s_{NN}} = 7$ TeV versus the ALICE data (black symbols) from Ref. [7]. The K^* momenta have been obtained by reconstruction from the final $\pi + K$ mesons. As mentioned above, the final hadronic interaction in $p + p$ collisions is very small, thus the reconstructed and decay spectra for $p + p$ collisions are practically identical. As seen from Fig. 9, the elementary spectra are rather well reproduced by PHSD which provides a solid basis for the interpretation of the heavy-ion results, too.

We recall that $p + p$ collisions in the PHSD are based on the PYTHIA event generator [71].

B. Comparison of the PHSD results with experimental data

We now step on to a comparison of PHSD results for strange vector mesons from heavy-ion collisions with experimental observables at the LHC energy. To compare with the experimental data, we have used the experimental reconstruction method for the theoretical spectra by matching the four-momentum of the final pions and (anti)kaons stemming from the same $K^*/\overline{K}^*$ decay vertex. As has been shown above, this implies that the final reconstructed spectra differ from the true or decay $K^*/\overline{K}^*$ spectra due to the final-state interaction in the hadronic phase. In Fig. 10 we compare PHSD results for the transverse momentum spectra $\frac{d^2N}{dy dp_T}$ of $(K^{*0} + \overline{K}^{*0})/2$ for Pb+Pb collisions at midrapidity ($|y| < 0.5$) with the ALICE data at a center-of-mass

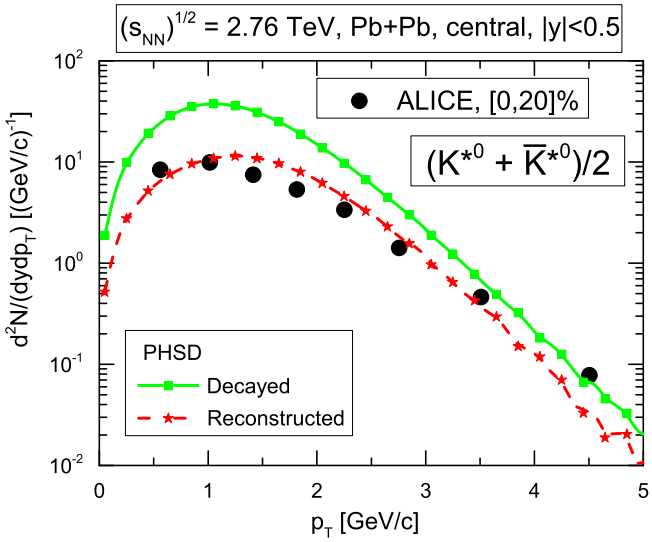

FIG. 8. The transverse momentum spectrum $d^2N/(dydp_T)$ of $(K^{*0} + \overline{K}^{*0})/2$ for a central Pb+Pb collision at midrapidity $|y| < 0.5$ and $\sqrt{s_{NN}} = 2.76$ GeV. The solid black circles show data from the ALICE collaboration [16], while the lines with symbols show the results from the PHSD: the solid green line with squares shows the spectrum calculated from K^*'s at the decay point while the dashed red line with stars shows the reconstructed spectrum from final (matching) (anti)kaons and pions.

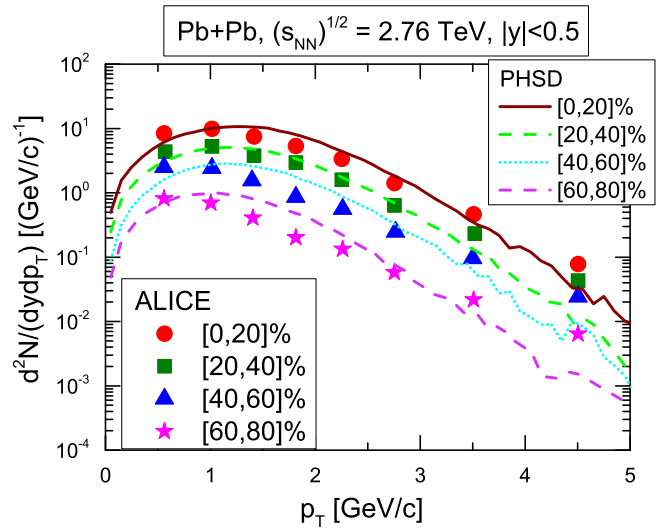

FIG. 10. The transverse momentum spectra $\frac{d^2N}{dydp_T}$ of $(K^{*0} + \overline{K}^{*0})/2$ as a function of the transverse momentum p_T for Pb+Pb collisions at midrapidity ($|y| < 0.5$) and $\sqrt{s_{NN}} = 2.76$ TeV for different centralities, ranging from very central to peripheral collisions. The lines correspond to results obtained from PHSD while the symbols represent experimental data from the ALICE collaboration [16]. The solid red circles correspond to a centrality of [0, 20]%, the red solid green squares correspond to a centrality of [20, 40]%, the solid blue triangles correspond to a centrality of [40, 60]% and the solid magenta stars correspond to a centrality of [60, 80]%. The solid dark red line corresponds to PHSD results for a centrality of [0, 20]%, the dashed green line corresponds to a centrality of [20, 40]%, the short-dotted light blue line corresponds to a centrality of [40, 60]%, and the dashed violet line corresponds to a centrality of [60, 80]%.

energy of $\sqrt{s_{NN}} = 2.76$ TeV for different centralities: [0–20]%, [20, 40]%, [40, 60]%, and [60, 80]%. As seen from Fig. 10 the PHSD calculations reasonably reproduce the ALICE data for all centralities at lower transverse momenta up to about $p_T \approx 3$ GeV/c, however they underestimate the high p_T part of the experimental spectra. This discrepancy for peripheral Pb+Pb collisions at large $p_T \geqslant 4$ GeV—in spite of a good agreement for pp collisions—can be understood as follows: in pp collisions K^*'s are produced directly from the string decays while in (semi)peripheral collisions, [60–80%], most K^*'s at midrapidity come from the $K + \pi$ annihilation; thus the final K^* spectra are sensitive to the "bulk dynamics" at larger p_T and less to the initial momentum distribution from strings. We note that in midrapidity (semi)peripheral collisions at LHC energies the energy density is very large and far above the critical energy density for the phase transition. Thus, in the overlapping region (i.e., midrapidity) of colliding nuclei, a QGP is formed. In the PHSD approach the properties of quarks and gluons are defined with the help of the DQPM model, which is fitted to the lQCD data in equilibrium, and depend only on temperature T. The same holds for the partonic interaction cross sections. The quark momentum distribution is transferred via hadronization to the mesons (pions, kaons, K^*'s etc.) and finally is reflected in K^*'s formed in the hadronic phase by $K + \pi$ annihilation. Thus, an underestimation of the slope of the final kaons and pions at large p_T in the PHSD is showing up in the underestimation of the K^*'s slope, too.

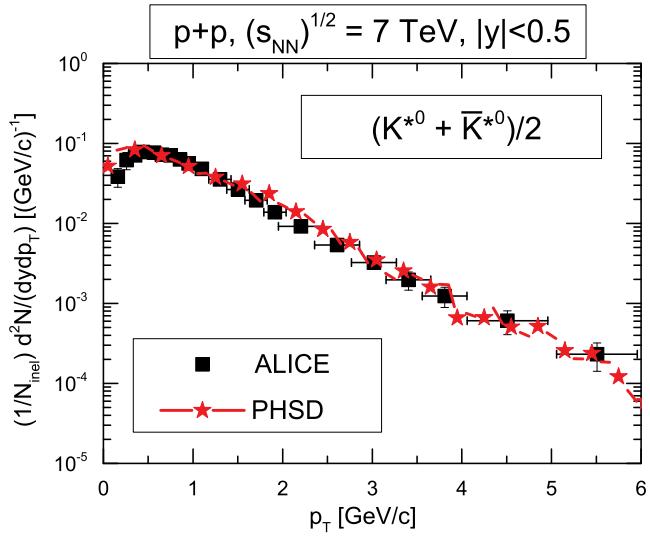

FIG. 9. The transverse momentum spectrum $\frac{1}{N_{\rm inel}}\frac{d^2N}{dydp_T}$ of $(K^{*0} + \overline{K}^{*0})/2$ mesons for $p + p$ collisions at midrapidity $|y| < 0.5$ at the LHC energy of $\sqrt{s_{NN}} = 7$ TeV. The line stands for the PHSD results while the black symbols show the experimental data from the ALICE collaboration [7].

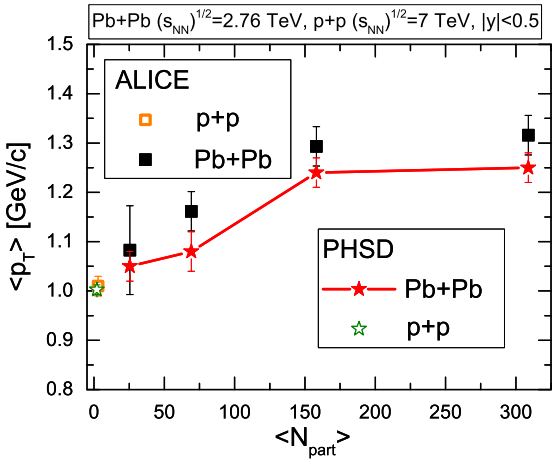

FIG. 11. The average transverse momentum $\langle p_T \rangle$ of $(K^{*0} + \overline{K}^{*0})/2$ as a function of the average number of participants $\langle N_{\rm part} \rangle$ for $p+p$ and Pb+Pb collisions at $\sqrt{s_{NN}} = 7$ TeV and $\sqrt{s_{NN}} = 2.76$ TeV, respectively. The solid red line with full stars stands for the PHSD results for Pb+Pb, the open star shows the PHSD result for $p+p$ collisions. Experimental data from the ALICE collaboration are shown as solid black squares for Pb+Pb and open squares for $p+p$ and taken from Ref. [16].

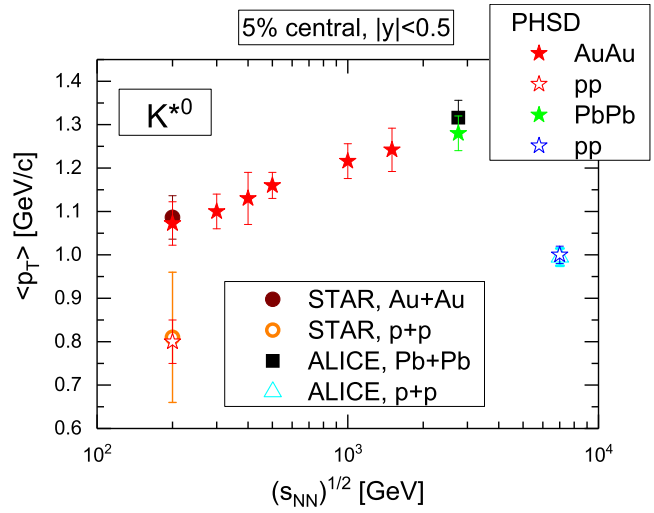

FIG. 12. The average transverse momentum $\langle p_T \rangle$ of K^{*0} as a function of the invariant center-of-mass energy $\sqrt{s_{NN}}$ ranging from central Au+Au collisions at RHIC energies up to central Pb+Pb and $p+p$ collisions at LHC energies. The PHSD results are shown as stars (open for $p+p$, solid for Au+Au/Pb+Pb), the full dot shows the STAR data, the full square shows ALICE data for Pb+Pb, and open square for $p+p$. The experimental data are taken from Ref. [16].

The information on the centrality dependence of the transverse spectra of $(K^{*0} + \overline{K}^{*0})/2$ can be viewed also in terms of the averaged $\langle p_T \rangle$ at each centrality bins. Figure 11 shows the average transverse momentum of the K^{*0} and $\overline{K}^{*0}$ mesons from the PHSD calculations for Pb+Pb at midrapidity as a function of the average number of participants $\langle N_{\rm part} \rangle$ in comparison to the ALICE data [16]. Also the results for $p+p$ collisions is shown. One can see that the average $\langle p_T \rangle$ grows from $p+p$ to peripheral and to central collisions and then saturates. The PHSD results are in good agreement with the ALICE measurements.

Figure 12 shows the average transverse momentum $\langle p_T \rangle$ of the K^{*0} and $\overline{K}^{*0}$ from the PHSD calculations as a function of the center-of-mass energy $\sqrt{s_{NN}}$—from RHIC to LHC—for $p+p$ and Au+Au/Pb+Pb collisions in comparison to the experimental data from STAR and ALICE. One can see that the experimental data show that $\langle p_T \rangle$ from central Au+Au/Pb+Pb is larger than those from $p+p$ for both (RHIC and LHC) energies; on the other hand the $\langle p_T \rangle$ grows with the energy for $p+p$ as well as heavy-ion collisions. These tendencies are reproduced by the PHSD calculations which predict a monotonic increase of $\langle p_T \rangle$ with energy.

Now we step to the particle ratios: we show in Fig. 13 the K^{*0}/K^- ratios as a function of $[dN(ch)/d\eta]^{1/3}$ for $p+p$ and Pb+Pb collisions at LHC energies of $\sqrt{s_{NN}} = 7$ TeV and $\sqrt{s_{NN}} = 2.76$ TeV, respectively. The results from PHSD (using a reconstruction method for K^{*0} and applying the experimental cuts on the mass of K^*) are compared to experimental data from the ALICE collaboration [16]. The experimental as well as theoretical ratios decrease with increasing centrality due to the stronger final state interaction effect in central collisions compared to peripheral reactions. Since the hadron density is large in the central region at the LHC, the K^-'s as well as the pions and kaons from K^{*0} decays rescatter very often. We note that the meson rescattering and absorption effects are stronger at LHC than at RHIC which leads to the decrease of the K^{*0}/K^- ratios at LHC for central collisions compared to a rather flat ratio at RHIC (cf. Fig. 15 in [37]).

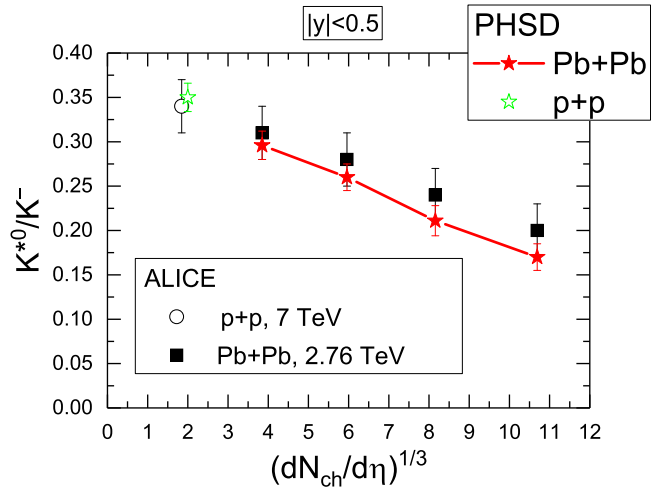

FIG. 13. The particle ratio K^{*0}/K^- vs $(dN_{ch}/d\eta)^{1/3}$ for $p+p$ and Pb+Pb collisions at the LHC energies of $\sqrt{s_{NN}} = 7$ TeV and $\sqrt{s_{NN}} = 2.76$ TeV, respectively. The PHSD results are shown by the red line with starts for central Pb+Pb and the open star for $p+p$ collisions. The experimental data from the ALICE collaboration are displayed as solid squares for Pb+Pb and the open dot for $p+p$ as taken from Ref. [16].

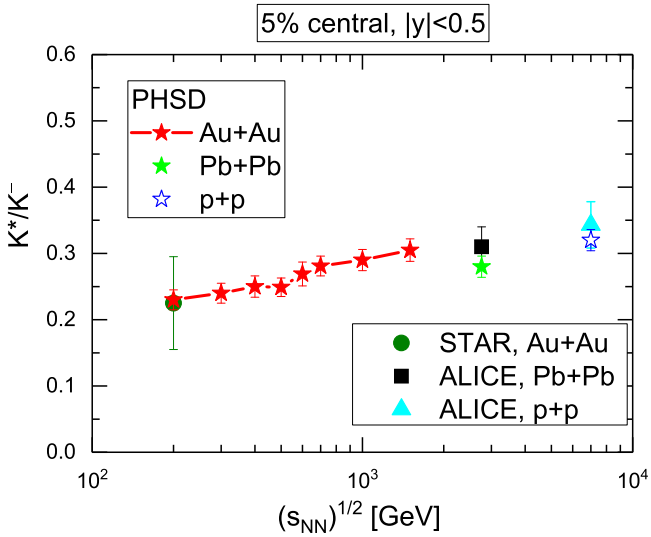

FIG. 14. The particle ratio K^{*-}/K^{-} as a function of the invariant center-of-mass energy $\sqrt{s_{NN}}$ ranging from central Au+Au collisions at RHIC energies up to central Pb+Pb collisions at the LHC energy of $\sqrt{s_{NN}} = 2.76$ TeV. The PHSD results are shown by the stars (open for $p+p$, solid for Au+Au/Pb+Pb, connected by the red line); the full dot shows the STAR data, the full square corresponds to ALICE data for Pb+Pb, and full triangles for $p+p$. The experimental data are taken from Ref. [16].

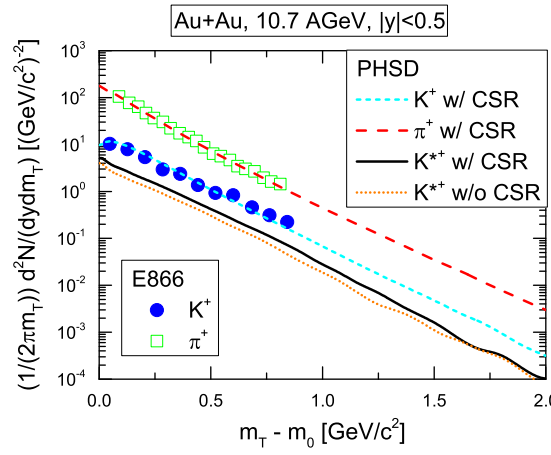

FIG. 15. Transverse mass spectra $1/(2\pi m_T)dN/dm_T$ as a function of the reduced transverse mass $m_T - m_0$ for central Au+Au collisions at bombarding energy of $E = 10.7$ AGeV at midrapidity ($|y| < 0.5$). The lines show results from PHSD while the symbols show experimental data from the E866 collaboration [74]. The solid blue circles display experimental data for K^+ while the open green squares show the experimental data for π^+ mesons. The corresponding theoretical results from PHSD including chiral symmtery restoration (CSR) are the light blue short-dashed line for the K^+ and the red dashed line for the π^+. The solid black line shows the results for the K^{*+} with CSR turned on in PHSD while the short-dotted orange line shows results for the K^{*+} without including CSR.

Furthermore, Fig. 14 shows the PHSD calculations for the K^{*-}/K^{-} ratio as a function of the invariant center-of-mass energy energy $\sqrt{s_{NN}}$ ranging from central Au+Au collisions at RHIC energies up to central Pb+Pb collisions at LHC energies in comparison to the experimental data from STAR (full dot) and ALICE (full square for Pb+Pb and full triangle for $p+p$). One can see that the ratio very smoothly increases with energy and is larger for $p+p$ than for Pb+Pb at LHC. That is due to a practically negligible final-state interaction in $p+p$ compared to Au+Au/Pb+Pb collisions.

VI. PREDICTIONS FOR FAIR/NICA

In the this section we show the results from the PHSD for strange vector meson production at much lower energies—from a few AGeV to few tens of AGeV, which will be achievable by the future FAIR and NICA or the BES program at RHIC. This energy range is very interesting for the following reasons:

(i) An interplay between the deconfined and chiral transitions is expected to happen in this energy range. Recently, the consequences of the chiral symmetry restoration (CSR) on observables in HICs has been studied within the PHSD approach [72,73]. The CSR has been incorporated in the PHSD via the Schwinger mechanism for the quark-antiquark production in the string decay and related to the dressing of the quark masses in the medium due to a linear coupling to the quark condensate $\langle\bar{q}q\rangle$. It has been shown that the inclusion of CSR effects provides a microscopic explanation for the "horn" structure in the excitation function of the K^+/π^+ ratio: the CSR in the hadronic phase produces the steep increase of this particle ratio up to $\sqrt{s} \sim 7$ GeV, while the drop at higher energies is associated to the appearance of a deconfined partonic medium. In this section we additionally investigate the effect of CSR on the production of the strange vector mesons K^* and $\overline{K}^*$.

(ii) At FAIR/NICA energies the medium effects—related to the modification of hadron properties at high baryon densities—are expected to be more visible than at RHIC or LHC energies due to the slower fireball expansion and larger net-baryon densities achieved—cf. Fig. 4. Thus, we investigate here the energy range which would be most appropriate for a study of the in-medium effects with K^*, $\overline{K}^*$ mesons.

We start by showing the m_T- and rapidity spectra of K^{*0} and $\overline{K}^{*0}$ mesons for central Au+Au collisions calculated with and without CSR effects at a center-of-mass energy of $\sqrt{s_{NN}} = 4.765$ GeV which is equivalent to the laboratory energy of $E = 10.7$ A GeV—cf. Figs. 15 and 16. Here the experimental data (from the E866 collaboration) are also available for pions and kaons [74].

As seen from Figs. 15 and 16 the PHSD calculations provide a good description of pion and kaon spectra when the CSR effect is included; we refer the reader to the detailed study on this issue in Refs. [72,73]. The inclusion of the CSR increases the yield of K^{*0} and $\overline{K}^{*0}$ by about 15–20%. That

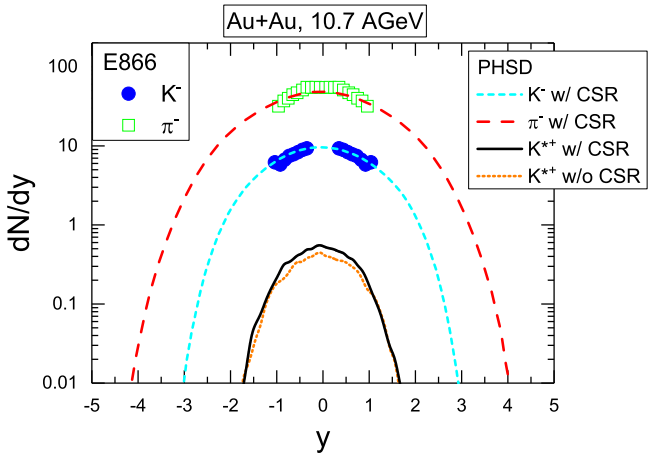

FIG. 16. Rapidity spectra dN/dy vs the rapidity y for a Au+Au collision at bombarding energy of $E = 10.7$ AGeV. The lines show results from PHSD while the symbols display experimental data from the E866 collaboration [74]. The solid blue circles show data for the K^- mesons while the open green squares show data for π^-. The corresponding theoretical results from PHSD are the light blue short-dashed line for the K^- and the red dashed line for the π^- mesons. The solid black line shows the results for the K^{*-} with CSR included while the short-dotted orange line shows results for the K^{*-} without CSR.

is mainly due to the increase of the kaon and antikaon yield when including the CSR.

Now we step to the results with the in-medium modifications of strange vector mesons. In Fig. 17 we show the PHSD predictions for the rapidity distributions (reconstructed y spectra) and in Figs. 18 and 19 for the p_T spectra as well as the mass distribution (decayed and reconstructed spectra) of $K^* = K^{*+} + K^{*0}$ [(a) and (c)] and $\overline{K}^* = K^{*-} + \overline{K}^{*0}$ [(b) and (d)] for central Au+Au collisions at bombarding energies of 4.5, 6, 8, 10.7, and 15 A GeV. The p_T spectra and mass distributions are calculated at midrapidity ($|y| < 0.5$). The dashed lines show the PHSD results without including the in-medium effects for K^* and $\overline{K}^*$ while the solid lines stand for the case with in-medium effects. We note that all calculations are performed with including the CSR effects.

As seen from Figs. 17–19, the in-medium effects on p_T and y spectra and the mass distribution increase with decreasing energy. This is due to the longer reaction time and slower expansion of the fireball at low energies such that the following occur:

(i) The strange vector mesons are still produced in a baryon rich environment (cf. Fig. 4) which leads to a pronounced modification of their spectral functions (cf. Fig. 1). The in-medium effects are stronger for the $\overline{K}^*$ than for the K^* for all energies as expected from Fig. 1 which shows the substantial modification of the $\overline{K}^*$ spectral function comparing in-medium and free cases and only modest modifications of K^* spectral functions. The pole of the in-medium $\overline{K}^*$ spectral function is shifted to the low mass range due to the attractive interaction of $\overline{K}^*$ with the baryonic medium while the pole of the K^* spectral function moves slightly to higher masses due to the repulsive interaction.

(ii) The decay of K^*, $\overline{K}^*$'s occurs in the hadronic medium such that the final mesons–(anti)kaons and pions—rescatter with hadrons or are absorbed which leads to the distortion of the reconstructed K^* spectra due to the final state iteration of the decay products—as discussed in Sec. V A—especially at low p_T. Again, the final K^-, $\overline{K}^0$ are interacting stronger with baryons than K^+, $\overline{K}^0$. The influence of the final state hadronic interaction on the modification of the spectra is illustrated in Fig. 20 which shows the ratio of reconstructed to decayed p_T spectra of $K^* = K^{*+} + K^{*0}$ (solid lines) and $\overline{K}^* = K^{*-} + \overline{K}^{*0}$ (dashed lines) for central Au+Au collisions at bombarding energies of 4.5, 6, 8, 10.7, and 15 A GeV for the case with in-medium effects as presented in Fig. 18. One can

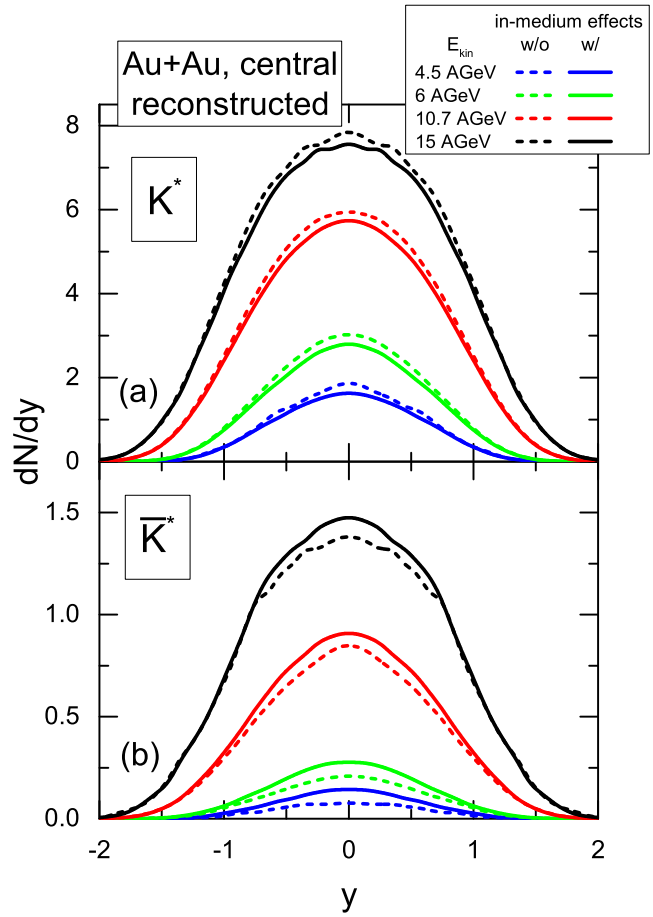

FIG. 17. PHSD predictions for the reconstructed rapidity spectra of $K^* = K^{*+} + K^{*0}$ (a) and $\overline{K}^* = K^{*-} + \overline{K}^{*0}$ (b) for central Au+Au collisions at bombarding energies of 4.5, 6, 8, 10.7, and 15 A GeV. The dashed lines show the PHSD results without including the in-medium effects for K^* and $\overline{K}^*$ while the solid lines correspond to the case with in-medium effects.

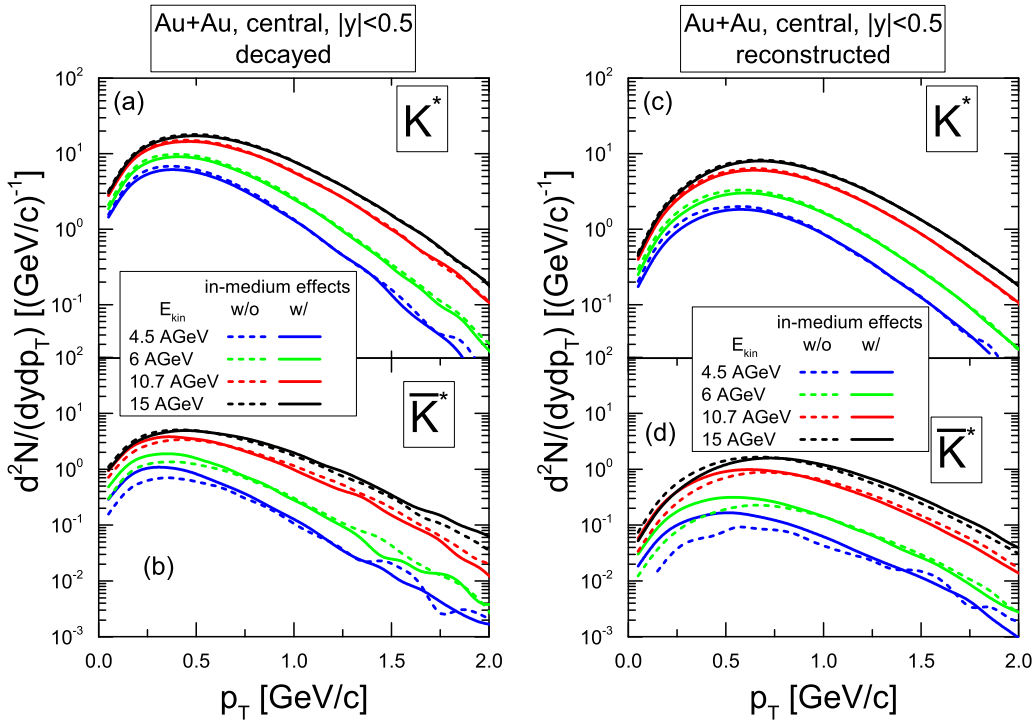

FIG. 18. PHSD predictions for the decayed (left) and reconstructed (right) p_T spectra of $K^* = K^{*+} + K^{*0}$ (a),(c) and $\overline{K}^* = K^{*-} + \overline{K}^{*0}$ (b),(d) for central Au+Au collisions at midrapidity ($|y| < 0.5$) at bombarding energies of 4.5, 6, 8, 10.7, and 15 A GeV. The dashed lines show the PHSD results without including the in-medium effects for K^* and $\overline{K}^*$ while the solid lines stand for the case with in-medium effects.

clearly see that rescattering of the final pions and kaons strongly affects the low p_T part of the $K^*, \overline{K}^*$ spectra and it is larger for $\overline{K}^*$.

As follows from Fig. 18 a sizable in-medium modification of the p_T spectra of $\overline{K}^*$'s is expected with decreasing bombarding energies: the p_T distribution is shifted to the low p_T region, such that the shift is about 0.1–0.15 GeV at 4.5 A GeV. Contrary to the $\overline{K}^*$ mesons, the p_T spectra of K^*'s are only slightly shifted to the high p_T region. Such shifts can be observed experimentally, e.g., by comparing the K^* with $\overline{K}^*$ spectra. Figure 21 shows the ratios of the reconstructed p_T spectra of K^* over $\overline{K}^*$ for central Au+Au collisions at midrapidity ($|y| < 0.5$) at bombarding energies of 4.5, 6, 8, 10.7, and 15 A GeV. The dashed lines show the PHSD results without including the in-medium effects for K^* and $\overline{K}^*$ while the solid lines stand for the case with in-medium effects. One can see that the ratio $K^*/\overline{K}^*$ is approximately flat over p_T for the in-medium cases while it decreases at low p_T strongly, especially at low energy.

In-medium effects are even more pronounced when looking at the mass distribution in Fig. 19. The shape of the $\overline{K}^*$ mass spectra (even integrated over all p_T as shown in Fig. 19) are strongly modified—it is getting flat at low M with decreasing bombarding energy. This is mainly due to the in-medium modification of the $\overline{K}^*$ spectral functions and final state interaction of the decay products. Here the modification of the reconstructed K^* mass distribution is less visible than for $\overline{K}^*$'s. The medium distortion of the $K^*/\overline{K}^*$ reconstructed mass spectra are stronger at low p_T, thus one can study experimentally the mass distribution of $K^*/\overline{K}^*$'s at different p_T bins. Figure 22 shows the PHSD predictions for the ratios of the reconstructed mass distribution of K^* over $\overline{K}^*$ for central Au+Au collisions at midrapidity ($|y| < 0.5$) at bombarding energies of 4.5, 6, 8, 10.7, and 15 A GeV. Here again the dashed lines show the PHSD results without including the in-medium effects for K^* and $\overline{K}^*$ while the solid lines stand for the case with in-medium effects. One can see the strong enhancement of the ratio for $M < 1$ GeV/c^2 for the in-medium scenarios while at larger p_T the differences are small.

Finally, we conclude that the future facilities—FAIR in Darmstadt as well as NICA and the fixed target BMN experiment at the Nuclotron in Dubna as well as the BES program at RHIC—are well located in energy to study the in-medium effects related to high baryon density, in particular the in-medium modification of the $K^*/\overline{K}^*$ spectral function. We note, however, that it is a rather challenging experimental task: in spite of the background being smaller at FAIR/NICA energies than at LHC or RHIC due to the lower pion and kaon abundances, the true signal is also smaller, and the final state interaction of the decay products is still large. We will discuss in the next section how to perform the experimental analysis of the mass spectra in order to obtain the in-medium signal.

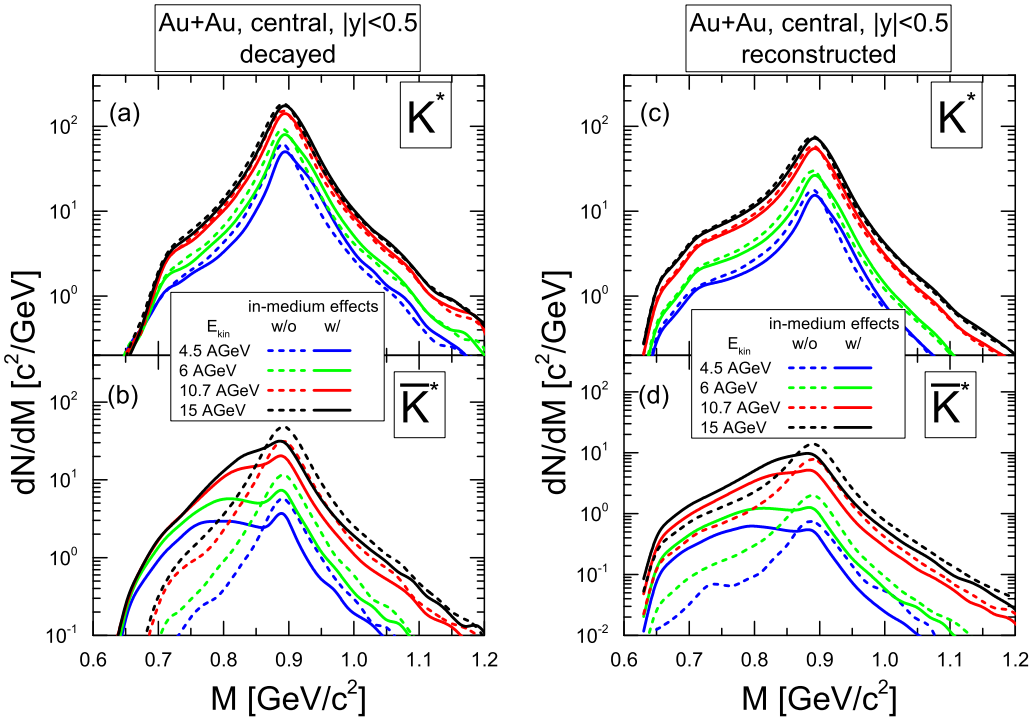

FIG. 19. PHSD predictions for the decayed (left) and reconstructed (right) mass distribution of $K^* = K^{*+} + K^{*0}$ (a),(c) and $\overline{K}^* = K^{*-} + \overline{K}^{*0}$ (b),(d) for central Au+Au collisions at midrapidity ($|y| < 0.5$) at bombarding energies of 4.5, 6, 8, 10.7, and 15 A GeV. The dashed lines show the PHSD results without including the in-medium effects for K^* and $\overline{K}^*$ while the solid lines stand for the case with in-medium effects.

VII. EXPERIMENTAL PROCEDURE TO EXTRACT MASS AND WIDTH OF A RESONANCE

A. Invariant mass distributions of decayed and reconstructed K^{*0} and $\overline{K}^{*0}$

In this section we present the experimental method to obtain information about the properties of resonances in the medium. We base our study on the PHSD results (without and with an in-medium modification) which are treated in a similar way as real experimental data. Using the PHSD as a "theoretical laboratory" we discuss the consequences of applying different experimental conditions, kinematic selections, and statistical errors from the underlying combinatorial background. We will present four different fit conditions and add the experimental procedure to it step by step.

Recall that experimental mass and width measurements of the $K^{*0} + \overline{K}^{*0}$ at LHC and RHIC energies show a mass shift in the low momentum region for heavy-ion collisions [4,5,16]. In order to shed light on the physical origin of this experimental observation, we investigate the mass and width of the K^{*0} and $\overline{K}^{*0}$ mass distribution from the PHSD approach calculated first at the decay point (decayed) and apply the reconstruction procedure to the final state particles—pions and kaons—(reconstructed) as discussed in the previous sections. In the next step we account for the statistical error in the experimental data. Furthermore, we compare the PHSD results with measure the K^{*0} and $\overline{K}^{*0}$ from data from the ALICE experiment. We note that for the PHSD results we use the 0–5% most central Pb-Pb collisions at $\sqrt{s_{NN}} = 2.76$ TeV.

Definition of four different fit procedures

The mass and width information of the resonances is obtained from the measured differential invariant mass spectra dN/dM. One has to keep in mind that invariant mass spectra of resonances contain the information on the spectral function as well as on the occupation probability. Since both parts of the information cannot be separated experimentally from the measured spectra, one has to apply some assumptions. The

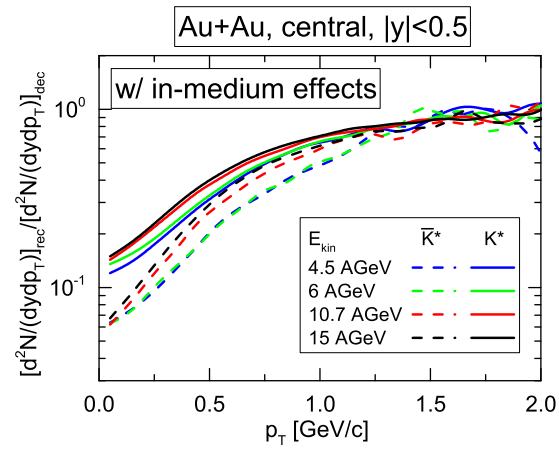

FIG. 20. The ratio of reconstructed to decayed p_T spectra of $K^* = K^{*+} + K^{*0}$ (solid lines) and $\overline{K}^* = K^{*-} + \overline{K}^{*0}$ (dashed lines) for central Au+Au collisions at bombarding energies of 4.5, 6, 8, 10.7, and 15 A GeV for the case with in-medium effects.

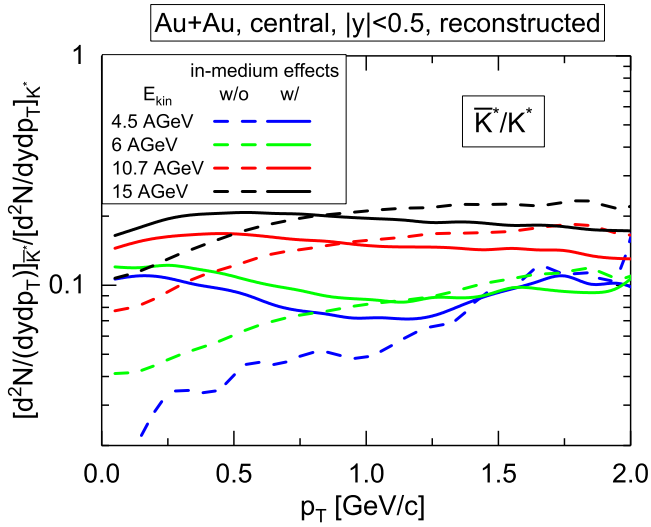

FIG. 21. PHSD predictions for the ratios of the reconstructed p_T spectra of $\overline{K}^*$ over K^* for central Au+Au collisions at midrapidity ($|y| < 0.5$) at bombarding energies of 4.5, 6, 8, 10.7, and 15 A GeV. The dashed lines show the PHSD results without including the in-medium effects for K^* and $\overline{K}^*$ while the solid lines stand for the case with in-medium effects.

simplest approximation is to assume that the resonances are produced in the equilibrated medium with a spectral function of Breit-Wigner form, i.e., the resonance mass spectrum is proportional to the Breigt-Wigner spectral function A, as defined in Sec. III, Eq. (4), weighted by a thermal Boltzmann distribution with temperature T. If one wants to differentiate the information further and account for the p_T dependence, e.g., to consider the mass spectra in some p_T interval, the

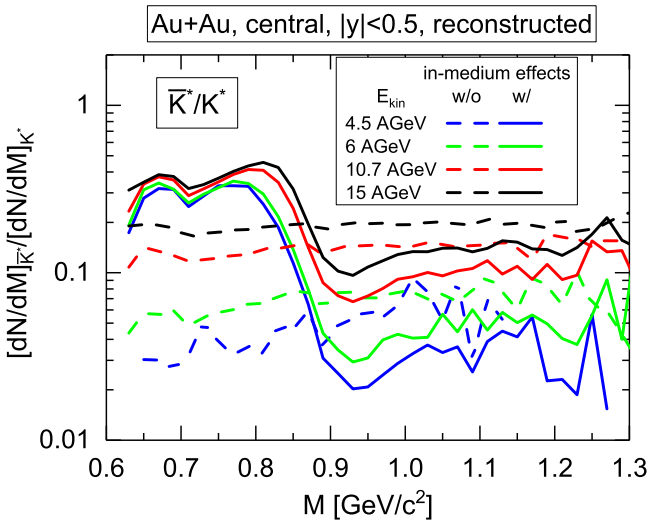

FIG. 22. PHSD predictions for the ratios of the reconstructed mass distribution of $\overline{K}^*$ over K^* for central Au+Au collisions at midrapidity ($|y| < 0.5$) at bombarding energies of 4.5, 6, 8, 10.7, and 15 A GeV. The dashed lines show the PHSD results without including the in-medium effects for K^* and $\overline{K}^*$ while the solid lines stand for the case with in-medium effects.

general form of the fit function F is defined as follows:

$$F(M|C, M_V^*, \Gamma_V^*, p_T, T) = A(M|C, M_V^*, \Gamma_V^*) f(M|p_T, T). \tag{9}$$

The notation $F(X|X_1, X_2, \ldots, X_N)$ means that one fits the X distribution by varying the parameters $X_1, X_2, \ldots, X_N$. In Eq. (9) the $A(M|C, M_V^*, \Gamma_V^*)$ is a relativistic mass-dependent Breit-Wigner function for the strange vector resonance $V = K^{*0}$ or $\overline{K}^{*0}$, given by

$$A(M|C, M_V^*, \Gamma_V^*) = C \frac{M^2 \Gamma_V^*}{\left(M^2 - M_V^{*2}\right)^2 + (M\Gamma_V^*)^2}. \tag{10}$$

For all fit cases considered below, the overall scale (C) and the mass peak (M_V^*) are free fit parameters. The quantity Γ_V^* represents the total mass dependent width of the V resonance in the medium which relates to the imaginary part of the self-energy in line with Eq. (7). However, for the experimental fit one adopts an approximation that the total mass dependent width in the spectral function can be expressed as a sum of the decay and collisional widths:

$$\Gamma_V^*(M) = \Gamma_{V,\mathrm{dec}}(M) + \Gamma_{\mathrm{coll}}, \tag{11}$$

where the mass dependent decay width of a strange vector resonance V is defined by Eq. (2) by assuming that the kaon spectral function can be replaced by the δ function, i.e., by ignoring the in-medium modification of the kaon properties. Thus,

$$\Gamma_{V,\,\mathrm{dec}}(M) = \Gamma_V^0 \left(\frac{M_V}{M}\right)^2 \left(\frac{q(M)}{q(M_V)}\right)^3. \tag{12}$$

Here, the momentum of the V resonance with mass M is $q(M) = \sqrt{\lambda(M, M_K, M_\pi)}/2M$. The vacuum width and mass of the K^{*0} and $\overline{K}^{*0}$ used for our fit is chosen to be the same as in the theoretical calculations: $\Gamma_V^0 = 42$ MeV and $M_V = 892$ MeV; M_K is the kaon mass (493.7 MeV) and M_π is the pion mass (139.6 MeV). In Eq. (9) Γ_{coll} stands for the collisional width which accumulates the effects of the in-medium modification to the total width and is one of the fit parameters.

Furthermore, in Eq. (9) $f(M|p_T, T)$ is the thermal Boltzmann factor:

$$f(M|p_T, T) = \frac{M}{\sqrt{M^2 + p_T^2}} \exp\left(-\frac{\sqrt{M^2 + p_T^2}}{T}\right), \tag{13}$$

which accounts for the exponential phase space distribution (spectrum) of the resonance.

We note that Eq. (13) follows from the Boltzmann distribution when neglecting the "thermal" motion of resonances (see, e.g., [75]) which could be an acceptable approximation for the midrapidity case and is commonly used by experimental collaborations [4,16]. A temperature of $T = 160$ MeV, which is close to the chemical freeze-out, is used for the resonances at the decay point and $T = 100$ MeV is used to describe the reconstructed resonance distribution close to the kinetic freeze-out. Before fixing T we perform a fit treating T as a free parameter. The temperature dependence in the fit is rather

small and we achieve a good χ^2 within 20 MeV around the selected fixed value for T.

For our fits, the width of the Breit-Wigner function is handled in three different ways: (1) In the first case, the mass dependent width case, the vacuum decay width depends on mass; the collisional width $\Gamma_{\rm coll}$ is the free fit parameter. (2) For the second case the fits are performed assuming the total width of the Briet-Wigner spectral function (Γ_V^*) is a free fit parameter. (3) Finally we consider a fixed width case, where the total width is fixed to the constant value 50 MeV.

We define four different fitting procedures to describe the theoretical spectra which are treated as experimental data by applying/adding the experimental conditions. The four fitting options are listed below where the colors in parentheses indicate the corresponding curves in the figures.

Fit I. Mass dependent width (black). A fit using the relativistic Breit-Wigner spectral function (10) with mass dependent width defined by Eqs. (11) and (12) with $\Gamma_{\rm coll}$ as a fit parameter. The Boltzmann factor (13) with $T = 160$ MeV (for the fit to decayed spectra) or $T = 100$ MeV (for the fit to reconstructed spectra) is employed using the statistical error strictly based on the theoretical counts ($\sqrt{N}$ for each bin).

Fit II. Mass dependent width +5% error (green). The same as fit I but 5% error bars are added to the theoretical calculations. This fit is used to mimic the fitting conditions used for data obtained at ALICE. For that we need to take into account the statistical errors present in the experimental data. Since the resonance mass peak sits on top of a large combinatorial background, the statistical errors of each bin in the resonance mass region are roughly the same (≈5% of the peak bin).

Fit III. Simple width +5% error (blue). A fit using the relativistic Breit-Wigner spectral function where the total width is a free parameter of the fit (no mass dependence). The Boltzmann factor is defined with $T = 160$ MeV (decayed) or $T = 100$ MeV (reconstructed). Additional 5% error bars are added for the PHSD calculations. We note that this "simple width" case is mostly used in the experimental fitting procedures.

Fit IV. Fixed vacuum width +5% error (red). A fit using the relativistic Breit-Wigner spectral function where the total width is fixed to the PHSD vacuum width of $\Gamma_0 = 42$ MeV/c^2. Also additional error bars of 5% are added to the theoretical calculations. We note that the experimental fit with a fixed width set to the vacuum value is used to search for any deviation from the vacuum widths. However, the χ^2 value of the fit turned out to be reasonable within the statistical error. For the RHIC and LHC data the width was fixed to the vacuum width of 50 MeV/c^2 to constrain the fit. This was done to stabilize the background (BG) fit to extract the resonance signal above the BG.

All fits have been performed within the invariant mass rage of 0.7 GeV/c^2 and 1.1 GeV/c^2.

B. K^{*0} and $\overline{K}^{*0}$ mass and width for different fit options

This PHSD calculations are done without the in-medium modification from CSR. Figure 23 shows the invariant mass distributions of the K^{*0} in the low momentum region ($p_{\rm T}$ = 0.4–0.6 GeV/c) at the decay point (left) and the reconstructed point (right). The reconstructed K^{*0} resonances show a broadening of the invariant mass distribution to lower masses. This will result in a width broadening of the signal and a possible mass shift as an effect from the hadronic phase interactions. The same is visible for the antiparticle $\overline{K}^{*0}$ shown in Fig. 24.

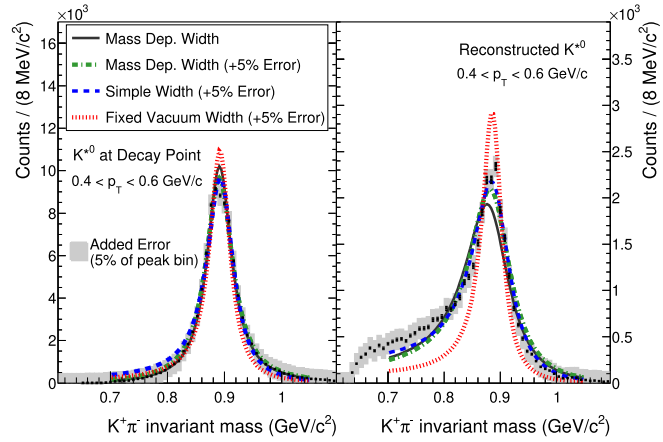

FIG. 23. Invariant mass distributions of the K^{*0} from the PHSD calculations (with no in-medium modification) in the low momentum region ($p_{\rm T}$ = 0.4–0.6 GeV/c) at the decay point (left) and for the reconstructed case (right).

We investigate the initial masses and width distributions of the K^{*0} (and $\overline{K}^{*0}$) due to the hadronic medium. This will answer the question as to how much of the initial vacuum spectral function is modified by the hadronic medium due to the hadronic interactions. In addition we investigate the effects of the experimental resonance signal extraction. And the statistical error on the experimental data due to the combinatorial background underneath the invariant mass signal is studied.

Figure 25 shows the K^{*0} (same for $\overline{K}^{*0}$) mass (left) and width (right) versus transverse momentum at the decay point

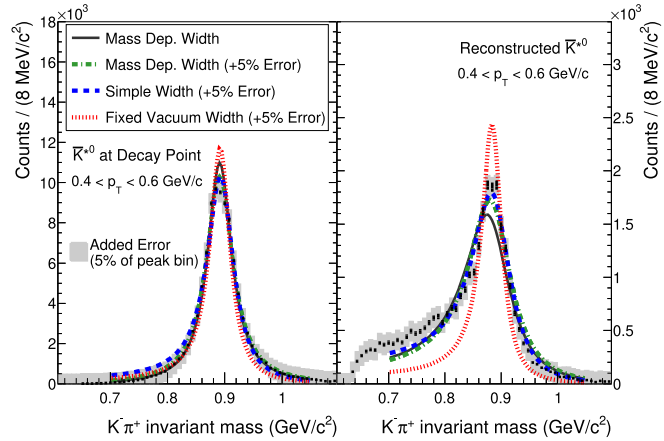

FIG. 24. Invariant mass distributions of the $\overline{K}^{*0}$ from the PHSD calculations (with no in-medium modification) in the low momentum region ($p_{\rm T}$ = 0.4–0.6 GeV/c) at the decay point (left) and for the reconstructed case (right).

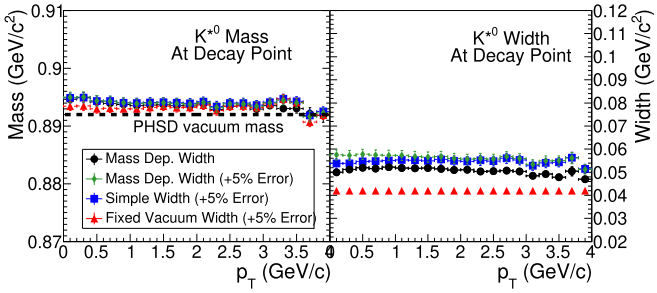

FIG. 25. Mass and width for the different fits of the K^{*0} (same for $\overline{K}^{*0}$) at the decay point. The PHSD vacuum mass is 0.892 GeV/c^2 and vacuum width is 42 GeV/c^2.

without in-medium modification. The PHSD vacuum values for the mass is 0.892 GeV/c^2 and for the width is 42 GeV/c^2. A clear mass shift to higher masses is visible for the K^{*0} and the width it is between $\Gamma_{K^{*0}} = 50$–60 MeV/c^2.

The reconstructed K^* resonances from the final state particles show a shift towards broader widths and smaller masses as shown in Fig. 26. The K^{*0} (the same for $\overline{K}^{*0}$) masses are shifted by 5–10 MeV/c^2 to lower masses in the low momentum region around $p_T = 1$ GeV/c. The widths are increased in the low momentum regions by 20–40 MeV/c^2.

This mass shift and width broadenings are effects from the hadronic phase interactions which change the spectral function shape. This is mainly due to the regeneration of the resonance at later times and lower temperatures, which populate preferentially the low mass region.

Figure 27 shows the ratios (left axis) of the reconstructed mass distributions of the K^{*0} and $\overline{K}^{*0}$ resonances to the mass distribution of the resonances at the decay point as a function of the invariant mass. The corresponding mass distributions are also presented (right axis): K^{*0} reconstructed—black line, decayed—brown line; $\overline{K}^{*0}$ reconstructed—olive line, decayed—green line. It is clearly noticeable that the resonance mass distributions are shifted to lower masses throughout their interactions in the medium. The signal loss for the reconstructible resonances are mainly caused by further interactions of the decay particles in the hadronic phase.

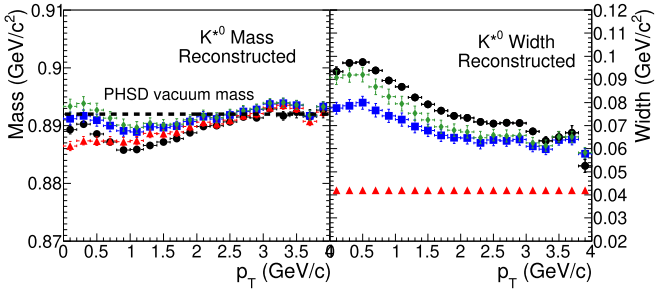

FIG. 26. Mass and width for the different fits of the K^{*0} (same for $\overline{K}^{*0}$) for the reconstructed resonance case. The PHSD vacuum mass is 0.892 GeV/c^2.

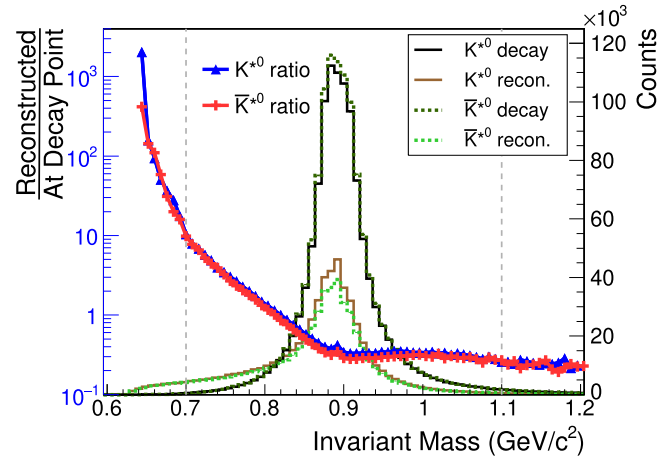

FIG. 27. Ratios (left axis) of the reconstructed mass distributions of the K^{*0} (blue) and $\overline{K}^{*0}$ (pink) resonances to the mass distribution at the decay point as a function of the invariant mass. The corresponding mass distributions are also presented (right axis): K^{*0} reconstructed—black line, decayed—brown line; $\overline{K}^{*0}$ reconstructed—olive line, decayed—green line. The results correspond to the PHSD calculations including no in-medium effects for the K^{*0} and $\overline{K}^{*0}$.

C. Comparison to experimental data

The comparison of the PHSD results (Fig. 26, red line) for the deviation from the vacuum mass of the fitted mass spectrum of reconstructed $K^{*0} + \overline{K}^{*0}$ mesons to the ALICE data [16] is shown in Fig. 28 as a function of the p_T. The ALICE data correspond to Pb+Pb, 0–20% most-central collisions at $\sqrt{s_{NN}} = 2.76$ TeV, while the PHSD data are from 0–5% Pb-Pb collisions. Since the vacuum mass value for the K^{*0} adopted in the PHSD is 892 MeV/c^2 and the PDF value is 895.81 MeV/c^2, we present the mass as a deviation from its

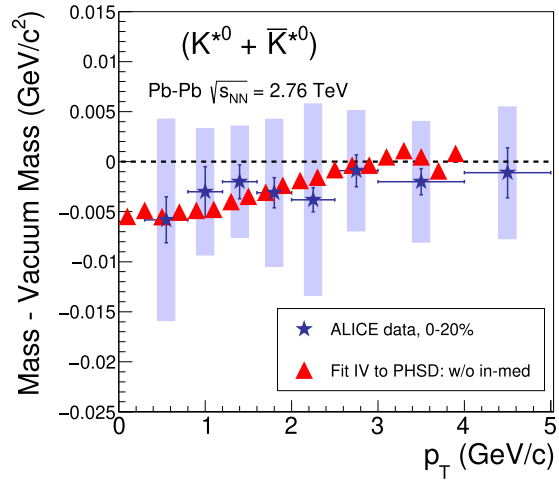

FIG. 28. Deviations from the vacuum mass for the ALICE data [16] and PHSD fitted mass spectrum of the reconstructed $K^{*0} + \overline{K}^{*0}$ as a function of p_T. The PHSD invariant mass distribution was fitted with fit IV (explained in the text) including statistical experimental error.

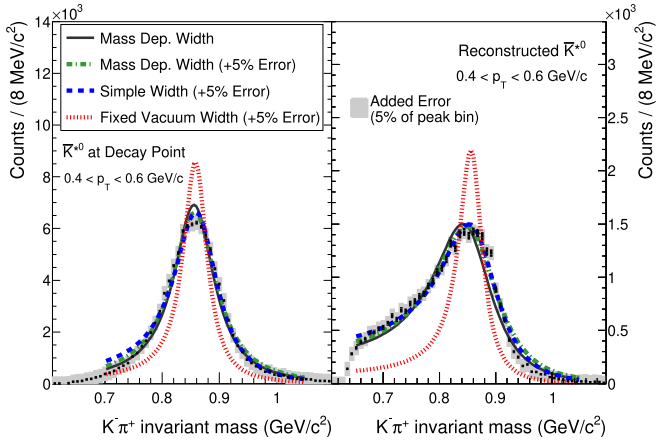

FIG. 29. Invariant mass distributions of the $\overline{K}^{*0}$ from the PHSD calculations (with in-medium effects) in the low momentum region ($p_T = 0.4$–0.6 GeV/c) at the decay point (left) and for the reconstructed case (right).

vacuum value. The vacuum width for the fixed width (fit IV) in the fit is 50 MeV/c^2 for the ALICE data and 42 MeV/c^2 in PHSD. The theoretical calculations describe the data very well within the statistical and systematical errors. At RHIC energies a similar but statistically more significant mass shift is visible [4,5]. According to the PHSD calculations the mass shift is caused by several effects. One is the K^* which survives that hadronic phase and the second is the fixed vacuum width fit. Remember the PHSD calculations here don't include the in-medium modification of the $K*/\overline{K}^*$ properties due to the coupling to baryonic medium discussed in Sec. III.

D. Estimation for mass shift from an in-medium modification

As follows from Fig. 28 the experimentally measured mass shift of strange vector mesons is reproduced by the PHSD and attributed to the interactions in the hadronic phase as well as to the resonance reconstruction procedure itself. In order to understand the sensitivity of our experimental procedure for the investigation of the medium effects, we perform a "model study" where we adopt an "extreme" in-medium scenario for $K^*/\overline{K}^*$ by considering the in-medium effects only due to the coupling to the baryonic medium and discarding the coupling to antibaryons. As discussed previously such a scenario cannot be realistic at the LHC energies due to the large antibaryon production rate at midrapidity which leads to a very low net-baryon density and small baryon chemical potential. This is contrary to FAIR/NICA energies where the matter is baryon dominated. However, this model study will help us get an idea for the sensitivity to measure the K^{*0} in-medium modification at LHC energies and answer the question of whether mass-shift signatures from in-medium effects would survive the interactions in the hadronic phase. Thus, we consider for our model study the in-medium modifications of $K^*/\overline{K}^*$ via coupling to the baryon density based on our in-medium scenario from Sec. III. Similar to low energies this will provide us a visible modification on the $\overline{K}^{*0}$ and very small change of K^{*0} since the baryon density itself is nonzero at the LHC energies contrary to the net-baryon density. With

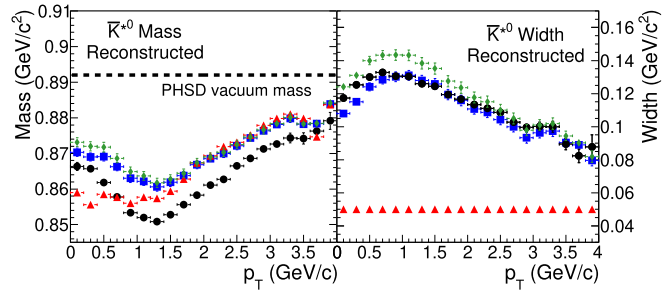

FIG. 30. Mass and width for the different fits of the $\overline{K}^{*0}$ for the reconstructed resonance case. The PHSD vacuum mass is 0.892 GeV/c^2.

this calculation we intend to simulate an upper limit for the possible in-medium signature.

Figure 29 shows the invariant mass distributions of the $\overline{K}^{*0}$ in the low momentum region ($p_T = 0.4$–0.6 GeV/c) at the decay point (left) and the reconstructed point (right). The $\overline{K}^{*0}$ at decay point already shows a wider distribution (compare to Fig. 24) due to the implementation of the in-medium effects. The reconstructed $\overline{K}^*$ resonances (right) from the final state particles show a shift toward broader widths and smaller masses. Figure 30 shows the corresponding $\overline{K}^{*0}$ mass shift of 20–30 MeV/c^2 to lower masses (left) and the width is increased to $\Gamma_{\overline{K}^{*0}} = 80$–$100$ MeV/c^2 in the low momentum region of $p_T = 0$–2 GeV/c.

The final comparisons to the experimental data are presented in Fig. 31 which shows the in-medium effects (open red triangles), which are very close to the calculation without the in-medium effects (solid red triangles). This shows that the presented way to "measure" the invariant mass of the $\overline{K}^{*0} + K^{*0}$ resonances are not very sensitive to the in-medium

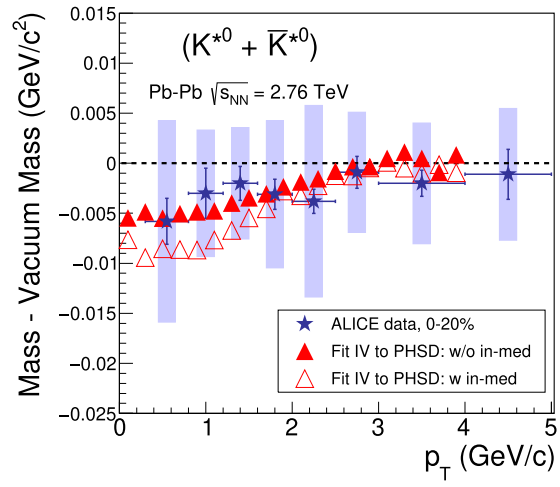

FIG. 31. Deviations from the vacuum mass for the ALICE data [16] and PHSD fitted mass spectrum of the reconstructed $K^{*0} + \overline{K}^{*0}$ as a function of p_T. The red solid triangles show the PHSD calculation without the in-medium modification and the red open triangles show the case for the in-medium modification. The PHSD invariant mass distribution was fitted with fit IV (explained in the text) including statistical experimental error.

scenarios. Even our "extreme" scenario for the in-medium modification shows only a 5 MeV/c^2 mass shift in the low momentum region from $p_T = 0$–1.5 GeV/c. The data are consistent with both scenarios due to their large error bars.

VIII. SUMMARY

We have studied the strange vector-meson dynamics (for K^* and $\overline{K}^*$) in $p + p$ and heavy-ion collisions at relativistic energies based on the in-medium effects and off-shell propagation from "G-matrix" calculations within the framework of the PHSD transport approach. We have used the self-energies obtained in our previous study [37] and implemented them in the form of mass shifts and widths into relativistic Breit-Wigner functions. On the basis of the widths and spectral functions we have implemented the resulting cross sections into the hadronization and $K\pi$ annihilation channels into PHSD for all isospin channels of the K^* and $\overline{K}^*$ mesons [29]. Since both the QGP and the hadronic phase are fully covered within the PHSD transport approach we have followed up the origin of the $K^*/\overline{K}^*$'s—created during the collision—as well as their properties. We have calculated differential spectra (as well as particle ratios) and compared the results to experimental data obtained by the ALICE collaboration at the LHC. Furthermore, we have also obtained results on $K^*/\overline{K}^*$ in-medium effects from PHSD for lower energies that create systems of higher net-baryon density and will be studied at the future FAIR and NICA.

Our findings are as follows:

(i) At LHC energies—similar to the RHIC energies—the main production channel of the $K^*/\overline{K}^*$ mesons is the resonant annihilation of $\pi + K(\overline{K})$ pairs in the final hadronic phase.

(ii) Only a small fraction of $K^*/\overline{K}^*$ mesons, which is created during the hadronization of the QGP, contributes to the final spectra.

(iii) At high energies, e.g., RHIC energies of $\sqrt{s_{NN}} =$ 200 GeV or LHC energies of $\sqrt{s_{NN}} = 2.76$ TeV, most $K^*/\overline{K}^*s$ are produced at rather low baryon densities. Consequently, in-medium effects on the $K^*/\overline{K}^*$ spectral functions do not play a big role.

(iv) On the other hand, the $K^*/\overline{K}^*$'s created at lower bombarding energies can probe net-baryon densities of up to $\rho/\rho_0 \approx 1.5$. This is due to the fact that many $K^*/\overline{K}^*$'s come from the annihilation of (anti)kaons and pions in the hadronic phase. Although $K^*/\overline{K}^*$'s are created at all stages in the collision, a few of them stem from high baryon-density regions.

(v) The medium at high energies expands very fast and only low baryon density regions can be reached because the system is dominated by the more abundant mesons rather than baryons. This is the case for RHIC and even more for LHC energies.

(vi) The PHSD results match the data for strange vector mesons in $p + p$ collisions at LHC energies very well.

(vii) The transverse momentum spectra in Pb+Pb collisions at LHC energies are reproduced very well in the lower transverse momentum region while the PHSD results show a softer spectrum in the high p_T region. Other observables like particle ratios and average momenta are in a reasonable agreement with experimental data.

(viii) Nevertheless, it is rather difficult to extract the $K^*/\overline{K}^*$ in-medium properties from the present experimental spectra at the LHC. By comparing the PHSD results for the true $K^*/\overline{K}^*$ spectra (calculated at the decay point of $K^*/\overline{K}^*$'s) with the reconstructed spectra [obtained by matching the final pions and (anti)kaons coming from the $K^*/\overline{K}^*$ decay], we have demonstrated how the distortion of the spectra occurs due to (1) the detector acceptance, the cuts in the invariant mass spectrum in the determination of the background spectra, and due to (2) the rescattering and absorption of the (anti)kaons and pions in the hadronic medium.

(ix) In spite of the difficulties discussed above we have presented experimental procedures to obtain the information on the medium effects by performing fits of the $K^*/\overline{K}^*$ reconstructed mass spectra and extracting the mass shift and in-medium widths. This will help us to interpret the experimental measurement on the mass shift.

(x) We have presented PHSD predictions for strange vector meson production at lower energies—from a few A GeV to few tens of A GeV, achievable by the future FAIR, NICA, and the BES program at RHIC. Here the expected in-medium effects are large, especially for $\overline{K}^*$'s, due to the longer reaction time and higher baryon densities at the production of $K^*/\overline{K}^*$. However, similar to the high energy regime of LHC and RHIC, the reconstructed spectra are distorted due to the final state interaction of final kaons and pions.

(xi) We find that the low momentum mass shift of $K^{*0} + \overline{K}^{*0}$ at LHC and RHIC energies is in agreement with the theoretical calculations based on the PHSD transport approach. The mass shift is dominated by the later hadronic interactions and the exact reconstruction method used, such that even in the extreme model of large coupling to a baryonic medium the overall mass shift is within experimental errors.

Thus, our present analysis for the LHC energies together with our early study in Ref. [37] for RHIC energies and our new predictions for the FAIR/NICA/BES-RHIC energies show that the $K^*/\overline{K}^*$ resonances are much better suited to probe the final hadronic phase rather than the QGP at freeze-out. Moreover, the distortion of the initial shape of the K^* spectra at the decay point compared to the final spectra (reconstructed from $\pi + K$ directly) indicates a strong final state interaction (rescattering and absorption) during the hadronic stage of HIC. We note that the influence of hadronic interactions on the final observables has been also discussed

in the recent study in Ref. [76]. Finally, the hadronic phase plays a dominant role for the $K^*/\overline{K}^*$ resonance dynamics in the heavy-ion collisions and has to be accounted for in the interpretation of the experimental results.

ACKNOWLEDGMENTS

The authors acknowledge inspiring discussions with J. Aichelin, W. Cassing, A. Knospe, P. Moreau, A. Palmese, T. Song, L. Tolos, and V. Voronyuk. A.I. acknowledges support by HIC for FAIR and HGS-HIRe for FAIR. This work was supported by BMBF, HIC for FAIR, and by the U.S. Department of Energy Office of Science under Contract No. DE-SC0013391. The computational resources have been provided by the LOEWE-CSC at the Goethe University Frankfurt. The authors acknowledge the Texas Advanced Computing Center (TACC) at the University of Texas at Austin for providing computing resources that have contributed to the research results reported within this paper [77].

[1] J. Rafelski, J. Letessier, and G. Torrieri, Phys. Rev. C **64**, 054907 (2001); **65**, 069902(E) (2002).
[2] C. Markert, G. Torrieri, and J. Rafelski, AIP Conf. Proc. **631**, 533 (2002).
[3] C. Markert, R. Bellwied, and I. Vitev, Phys. Lett. B **669**, 92 (2008).
[4] J. Adams *et al.* (STAR Collaboration), Phys. Rev. C **71**, 064902 (2005).
[5] M. M. Aggarwal *et al.* (STAR Collaboration), Phys. Rev. C **84**, 034909 (2011).
[6] L. Kumar (STAR Collaboration), EPJ Web Conf. **97**, 00017 (2015).
[7] B. Abelev *et al.* (ALICE Collaboration), Eur. Phys. J. C **72**, 2183 (2012).
[8] A. Pulvirenti (ALICE Collaboration), J. Phys. G **38**, 124077 (2011).
[9] A. Karasu Uysal (ALICE Collaboration), J. Phys.: Conf. Ser. **347**, 012012 (2012).
[10] A. Badala *et al.* (ALICE Collaboration), J. Phys.: Conf. Ser. **455**, 012003 (2013).
[11] M. Nicassio (ALICE Collaboration), EPJ Web Conf. **60**, 13006 (2013).
[12] A. G. Knospe (ALICE Collaboration), J. Phys.: Conf. Ser. **420**, 012018 (2013).
[13] A. G. Knospe (ALICE Collaboration), J. Phys.: Conf. Ser. **509**, 012087 (2014).
[14] S. Singha (ALICE Collaboration), PoS CPOD **2013**, 055 (2013), arXiv:1306.0673.
[15] A. G. Knospe (ALICE Collaboration), J. Phys.: Conf. Ser. **446**, 012056 (2013).
[16] B. B. Abelev *et al.* (ALICE Collaboration), Phys. Rev. C **91**, 024609 (2015).
[17] E. Fragiacomo (ALICE Collaboration), EPJ Web Conf. **81**, 04004 (2014).
[18] A. Badala (ALICE Collaboration), EPJ Web Conf. **66**, 04002 (2014).
[19] A. Ortiz (ALICE Collaboration), Nucl. Phys. A **956**, 757 (2016).
[20] F. Bellini (ALICE Collaboration), EPJ Web Conf. **97**, 00004 (2015).
[21] A. G. Knospe (ALICE Collaboration), J. Phys.: Conf. Ser. **612**, 012064 (2015).
[22] A. Badala (ALICE Collaboration), EPJ Web Conf. **95**, 04002 (2015).
[23] A. Badala (ALICE Collaboration), EPJ Web Conf. **96**, 01003 (2015).
[24] A. G. Knospe (ALICE Collaboration), EPJ Web Conf. **117**, 03002 (2016).
[25] J. Adam *et al.* (ALICE Collaboration), Eur. Phys. J. C **76**, 245 (2016).
[26] M. Bleicher and J. Aichelin, Phys. Lett. B **530**, 81 (2002).
[27] S. Vogel, J. Aichelin, and M. Bleicher, J. Phys. G **37**, 094046 (2010).
[28] A. G. Knospe, C. Markert, K. Werner, J. Steinheimer, and M. Bleicher, Phys. Rev. C **93**, 014911 (2016).
[29] A. Ilner, D. Cabrera, C. Markert, and E. Bratkovskaya, Phys. Rev. C **95**, 014903 (2017).
[30] M. Lutz, Phys. Lett. B **426**, 12 (1998).
[31] A. Ramos and E. Oset, Nucl. Phys. A **671**, 481 (2000).
[32] L. Tolos, A. Ramos, A. Polls, and T. T. S. Kuo, Nucl. Phys. A **690**, 547 (2001).
[33] L. Tolos, A. Ramos, and E. Oset, Phys. Rev. C **74**, 015203 (2006).
[34] M. F. M. Lutz, C. L. Korpa, and M. Moller, Nucl. Phys. A **808**, 124 (2008).
[35] L. Tolos, D. Cabrera, and A. Ramos, Phys. Rev. C **78**, 045205 (2008).
[36] O. Linnyk, E. L. Bratkovskaya, W. Cassing, Prog. Part. Nucl. Phys. **87**, 50 (2016).
[37] A. Ilner, D. Cabrera, P. Srisawad, and E. Bratkovskaya, Nucl. Phys. A **927**, 249 (2014).
[38] W. Cassing and E. L. Bratkovskaya, Nucl. Phys. A **831**, 215 (2009).
[39] E. L. Bratkovskaya, W. Cassing, V. P. Konchakovski, and O. Linnyk, Nucl. Phys. A **856**, 162 (2011).
[40] L. P. Kadanoff and G. Baym, *Quantum Statistical Mechanics* (Benjamin, New York, 1962).
[41] S. Juchem, W. Cassing, and C. Greiner, Nucl. Phys. A **743**, 92 (2004).
[42] W. Cassing, Nucl. Phys. A **795**, 70 (2007).
[43] W. Cassing, Nucl. Phys. A **791**, 365 (2007).
[44] Y. Aoki, S. Borsanyi, S. Durr, Z. Fodor, S. D. Katz, S. Krieg, and K. K. Szabo, J. High Energy Phys. 06 (2009) 088.
[45] M. Cheng, N. H. Christ, S. Datta, J. van der Heide, C. Jung, F. Karsch, O. Kaczmarek, E. Laermann, R. D. Mawhinney, C. Miao *et al.*, Phys. Rev. D **77**, 014511 (2008).
[46] W. Cassing, Eur. Phys. J.: Spec. Top. **168**, 3 (2009).
[47] W. Cassing, O. Linnyk, T. Steinert, and V. Ozvenchuk, Phys. Rev. Lett. **110**, 182301 (2013).
[48] W. Ehehalt and W. Cassing, Nucl. Phys. A **602**, 449 (1996).
[49] W. Cassing and E. L. Bratkovskaya, Phys. Rep. **308**, 65 (1999).
[50] B. Andersson, G. Gustafson, and H. Pi, Z. Phys. C **57**, 485 (1993).
[51] W. Cassing, L. Tolós, E. L. Bratkovskaya, and A. Ramos, Nucl. Phys. A **727**, 59 (2003).

[52] M. Bando, T. Kugo, and K. Yamawaki, Nucl. Phys. B **259**, 493 (1985).
[53] E. Oset and A. Ramos, Eur. Phys. J. A **44**, 445 (2010).
[54] E. Oset, A. Ramos, E. J. Garzon, R. Molina, L. Tolos, C. W. Xiao, J. J. Wu, and B. S. Zou, Int. J. Mod. Phys. E **21**, 1230011 (2012).
[55] M. Bando, T. Kugo, S. Uehara, K. Yamawaki, and T. Yanagida, Phys. Rev. Lett. **54**, 1215 (1985).
[56] M. Bando, T. Kugo, and K. Yamawaki, Phys. Rep. **164**, 217 (1988).
[57] M. Harada and K. Yamawaki, Phys. Rep. **381**, 1 (2003).
[58] U. G. Meissner, Phys. Rep. **161**, 213 (1988).
[59] L. Tolos, R. Molina, E. Oset, and A. Ramos, Phys. Rev. C **82**, 045210 (2010).
[60] J. Beringer *et al.* (Particle Data Group Collaboration), Phys. Rev. D **86**, 010001 (2012).
[61] E. Oset and A. Ramos, Nucl. Phys. A **635**, 99 (1998).
[62] N. Kaiser, P. B. Siegel, and W. Weise, Nucl. Phys. A **594**, 325 (1995).
[63] C. M. Ko and G. Q. Li, J. Phys. G **22**, 1673 (1996).
[64] K. Haglin, Nucl. Phys. A **584**, 719 (1995).
[65] J. L. Goity and H. Leutwyler, Phys. Lett. B **228**, 517 (1989).
[66] A. Schenk, Phys. Rev. D **47**, 5138 (1993).
[67] E. L. Bratkovskaya and W. Cassing, Nucl. Phys. A **807**, 214 (2008).
[68] G. Breit and E. Wigner, Phys. Rev. **49**, 519 (1936).
[69] C. Patrignani *et al.* (Particle Data Group), Chin. Phys. C **40**, 100001 (2016).
[70] G. Q. Li, C. M. Ko, and G. E. Brown, Nucl. Phys. A **611**, 539 (1996).
[71] B. Nilsson-Almqvist and E. Stenlund, Comput. Phys. Commun. **43**, 387 (1987).
[72] W. Cassing, A. Palmese, P. Moreau, and E. L. Bratkovskaya, Phys. Rev. C **93**, 014902 (2016).
[73] A. Palmese, W. Cassing, E. Seifert, T. Steinert, P. Moreau, and E. L. Bratkovskaya, Phys. Rev. C **94**, 044912 (2016).
[74] L. Ahle *et al.* (E866 and E917 Collaborations), Phys. Lett. B **476**, 1 (2000).
[75] E. V. Shuryak and G. Brown, Nucl. Phys. A **717**, 322 (2003).
[76] J. Steinheimer, J. Aichelin, M. Bleicher, and H. Stöcker, Phys. Rev. C **95**, 064902 (2017).
[77] http://www.tacc.utexas.edu.